Hydrous fluids down to the semi-brittle root zone of detachment faults in nearly amagmatic ultra-slow spreading ridges

Manon Bickert, Mathilde Cannat, D. Brunelli

Hydrous fluids down to the semi-brittle root zone of detachment faults in nearly amagmatic ultra-slow spreading ridges

Bickert[1*, †], M., Cannat[2], Brunelli, D.[1, 3]

[1] *Dipartimento di Scienze Chimiche e Geologiche, Università di Modena e Reggio Emilia, Modena, Italy.*

[2] *Université Paris Cité, Institut de Physique du Globe de Paris, CNRS-UMR 7154, France.*

[3] *IGAG-CNR, Istituto di Geologia Ambientale e Geoingegneria, Rome, Italy.*

*Corresponding author: Manon.Bickert@ifremer.fr

[†] now at Geo-Ocean, Univ Brest, CNRS, IFREMER, UMR6538, F-29280 Plouzané, France.

Abstract

At the Eastern part of the Southwest Indian Ridge (SWIR), plate divergence is accommodated by large offset normal faults, also called detachment faults, that exhume mantle-derived rocks on the seafloor. A third of the ultramafic samples dredged on- and off-axis in this nearly amagmatic ridge setting present amphibole-bearing secondary mineralogical assemblages indicative of hydration, and for the most part predating the growth of serpentine minerals. The deepest evidence of hydration is the occurrence of small amounts of syn-kinematic amphibole in microshear zones with strongly reduced grain size, which record deformation at high stress and high temperatures (>800°C) at the root zone of the detachment. The composition of these amphiboles is consistent with a hydrothermal origin, suggesting that seawater derived fluids percolated down to the root of detachment faults, at

the Brittle-Ductile Transition (BDT). We propose that the constant exhumation of new mantle material to the seafloor, and the limited lifetime of each detachment (1-3 Myrs) prevent a more pervasive deep hydration of mid-ocean ridge detachment root regions, as proposed at transform fault plate boundaries.

Keywords: Southwest Indian Ridge, plate boundary faulting, deformation processes, hydration, amphiboles, fluid-rock interaction, brittle-ductile transition.

1. Introduction

At slow spreading-ridges, large offset normal faults exhume serpentinized mantle-derived rocks on the seafloor (Cann et al., 1997; Cannat, 1993; Escartín et al., 2008; Sauter et al., 2013; Smith et al., 2006; Tucholke et al., 2008). These faults, also called detachment faults, dip steeply at depth (Chen et al., 2023; deMartin et al., 2007; Parnell-Turner et al., 2017) and emerge at low angle on the seafloor (Cannat et al., 2019; Smith et al., 2006), conferring them a convex-downward profile. Detachment faults root into ductile fresh peridotites in the deep axial lithosphere, and bring these rocks to shallower depths, where seawater-derived fluids circulate through cracks and fissures and along grain boundaries, leading to extensive hydration and alteration.

Fracturing associated with the development of faults is a key mechanism that focuses fluid flow through the lithosphere at the axis of slow-spreading ridges. The deep microseismicity recorded at slow spreading ridges suggests that detachment faults root at depths down to 12 km at the Mid-Atlantic Ridge (MAR; de Martin et al., 2007; Parnell-Turner et al., 2020) and to

15-20 km at the Southwest Indian Ridge (SWIR; Chen et al., 2023; Grevemeyer et al., 2019; Schlindwein and Schmid, 2016; Yu et al., 2018).

The permeability created by networks of microfractures formed due to cooling of the exhuming mantle, close to the brittle-ductile transition (BDT), may also enhance the hydrothermal alteration of peridotites (de Martin et al., 2004; Fruh-green et al., 2004; Rouméjon and Cannat, 2014). As fluids interact with the exhuming mantle, hydrous minerals form, such as serpentine, brucite, talc, chlorite, and amphibole ranging from tremolite to Mg-hornblende and pargasitic compositions (Fruh-green et al., 2004; Fumagalli et al., 2009). Experimental studies have related these mineralogical assemblages to specific temperature ranges (Bach et al., 2004; Escartin et al., 1997; Klein et al., 2009). Hydrated assemblages, particularly those rich in phyllosilicates, are generally weaker than the anhydrous paragenesis, especially olivine, and therefore decrease the strength along the fault ($\mu<0.6$; Escartín et al., 2003). Hydration reactions are indeed observed to control strain localization in the upper brittle lithosphere at the axis of slow-spreading ridges, where hydrothermal alteration is pervasive and and where the ultramafic rocks are extensively serpentinized (Boschi et al., 2006; Escartín et al., 2003; Picazo et al., 2012; Schroeder and John, 2004). Deeper in the lithosphere, below the serpentinized domain, both higher confining pressure and temperature lead to the transition from brittle to ductile deformation and are expected to prevent vigorous hydrothermal circulation.

The presence of hydrous fluids in peridotites deforming at BDT conditions is, however, supported by several petrological studies reporting syntectonic Mg-hornblende to pargasitic amphiboles in deformed peridotites from oceanic detachment faults (Albers et al., 2019; Bickert et al., 2021; Boschi et al., 2006; Patterson et al., 2021; Picazo et al., 2012; Schroeder and John, 2004), oceanic transform faults (Cannat and Seyler, 1995; Cipriani et al., 2009;

Kakihata et al., 2022; Kohli and Warren, 2020; Prigent et al., 2020), orogenic massifs and ophiolites (Hidas et al., 2016; Prigent et al., 2018; Vieira Duarte et al., 2020). Petrographically, these amphiboles predate serpentine, hence suggesting their crystallization to occur at temperatures higher than the serpentine stability limit (Schroeder & John, 2004; Boschi et al., 2006; Fumagalli et al., 2009; Cannat et al., 2012; Picazo et al., 2012; Patterson et al., 2021). Several microstructural studies also show that these amphiboles formed in a semi-brittle rheology composed of brittle orthopyroxene and mostly crystal-plastic olivine, which would be consistent with deformation conditions close to the BDT, at the root zone of trans-lithospheric faults (Cannat and Seyler, 1995; Kohli and Warren, 2020; Prigent et al., 2020; Vieira Duarte et al., 2020). The origin of the fluids involved has also been investigated, and proposed to be primarily hydrothermal (Patterson et al., 2021; Prigent et al., 2020; Vieira Duarte et al., 2020).

Here, we study high-temperature amphiboles found in ultramafic samples dredged in two nearly-amagmatic corridors at the eastern Southwest Indian Ridge (SWIR, 62-65°E; Cannat et al., 2006; Sauter et al., 2013). This area is characterized by a very low melt supply and has an axial seismogenic lithosphere at least 15 km-thick (Chen et al., 2023; Grevemeyer et al., 2019; Schlindwein and Schmid, 2016). Successive detachment faults with flipping polarity (flip-flop detachments; Reston, 2018; Reston & McDermott, 2011) accommodate most of the plate divergence (Sauter et al., 2013), which contrast with the longer-lived detachments forming corrugated surfaces on one flank of the ridge only, in more magmatic and faster spreading contexts (Cann et al., 1997; Escartín et al., 2017; MacLeod et al., 2002; Smith et al., 2006). Rocks recovered along the steep footwalls of these successive detachment faults are mainly variably serpentinized peridotites, with minor amounts of basalts and gabbros (Fig. 1; Sauter et al., 2013; Rouméjon et al., 2015). The earliest lithospheric deformation recorded in the

variably serpentinized samples collected in this region of the SWIR combines crystal-plastic and brittle mechanisms, with anastomosing zones of grain size reduction (GSR) formed under high stress (80-270 MPa) and high temperature conditions (>800°C; Fig. 2a, 3; Bickert et al., 2020; 2021). This heterogeneous high stress deformation has been interpreted as characteristic of the root zone of the axial detachment faults (Bickert et al., 2021) and is very different from the high temperature, low stress deformation microstructures expected in the asthenospheric mantle or in the deep lithosphere, and recorded by ultramafic samples from more magmatic detachments (Albers et al., 2019; Ceuleneer and Cannat, 1997; Harigane et al., 2016; Seyler et al., 2007). Among samples with GSR, a few contain small amounts of amphibole that crystallized during GSR formation (Fig. 3b-d). Our primary objective here is to better constrain the origin of the fluids that crystallized these amphiboles: are they derived from small amounts of water in the residual lherzolitic mantle or formed from hydrous magmatic fluids? Are they evidence for deep penetration of seawater-derived fluids? To this aim, we provide a detailed textural, microstructural, and chemical analysis of these amphiboles, and compare these results with those obtained from GSR-free, amphibole-bearing peridotite samples from the same region, in which amphiboles are more clearly of hydrothermal origin. This comparison leads us to discuss the suite of hydration processes in the magma-poor root of the eastern SWIR flip-flop detachment faults, and the similarities and differences with hydration processes that have been documented down to similar to greater depths in the root zone of oceanic transform faults (Brunelli et al., 2020; Cipriani et al., 2009; Prigent et al., 2020).

2. Diversity and estimated abundance of eastern SWIR amphibole-bearing ultramafic rocks

120 Of the 33 dredges of the *Smoothseafloor* cruise (Sauter et al., 2013), 24 recovered
121 amphibole-bearing, variably serpentinized ultramafic samples (Fig. 1; Table A1). Overall,
122 amphibole-bearing peridotites represent 34% of the samples collected from these 24 dredges
123 (Table A2). Peridotites with amphibole-bearing GSR zones were recovered in only 4 dredges
124 from the western nearly amagmatic corridor (DR08, DR10, DR14, DR17; Fig. 1 and Table A2).
125 The deformation of the primary minerals in these samples has been characterized in a
126 previous study (Bickert et al., 2021), finding that GSR zones develop in peridotites that show
127 the highest rates of a high stress (80 to 270 MPa), relatively high temperature (~800–1000 °C)
128 deformation episode. The variable degrees of this heterogeneous deformation were
129 described in four textural types, from A0 for the least deformed (kinked pyroxenes, weakly
130 deformed olivine, no GSR), to A3 for the most deformed (kinked pyroxenes, strongly plastically
131 deformed olivine, continuous GSR zones; Table A3).
132 In addition to samples with amphibole-bearing GSR zones (Fig. 2a and 3), we identified 3
133 other types of amphibole-bearing ultramafic samples: amphibole-bearing melt-impregnated
134 ultramafic samples (Fig. 2b), amphibole mylonites (Fig. 2c), and amphibole-bearing
135 serpentinized peridotites (Fig. 2d).
136 Amphibole-bearing, melt-impregnated samples occur in 21 dredges (Fig. 1; Table A2) and
137 are interpreted as resulting from the hydration of peridotites impregnated by basaltic melts
138 in the plagioclase stability field (Paquet et al., 2016). In hand specimen, amphibole-bearing
139 domains are grey to dark, commonly foliated, and clustered along pyroxenes (Fig. 2b).
140 The amphibole mylonites are strongly foliated, commonly showing brown amphibole
141 porphyroclasts with evidence of rolling structures (σ-shapes; Fig. 2c), and domains recording
142 a higher strain with fewer porphyroclasts and a finer-grained matrix (Fig. 2c). Amphibole
143 mylonites occur were sampled in only 3 dredges (DR27, DR33 and DR34; Fig. 2c, Table A2).

144 Dredges 33 and 34 sampled a moderately magmatic, corrugated detachment footwall (Fig. 1;
145 Cannat et al., 2009).
146 The fourth type of amphibole-bearing peridotites is composed of strongly serpentinized
147 peridotites, which is relatively common and found in 16 dredges (Fig. 1; Table A2). In hand
148 specimen, amphibole-bearing serpentinized samples show a dark greenish color (Fig. 2d).
149 Olivine is fully serpentinized and/or replaced by oxidized minerals, while pyroxenes are
150 partially replaced by amphibole (Fig. 2d).
151 Overall, samples with amphibole-bearing GSR zones account for only 2% of the ultramafic
152 samples recovered by dredging in the study area (Table A2). Amphibole-bearing melt-
153 impregnated peridotites, amphibole mylonites and amphibole-bearing serpentinized
154 peridotites respectively count for 20%, 2% and 10% (Table A2).
155

156 ## 3. Sampling and analytical methods

157 We selected 28 amphibole-bearing ultramafic samples for detailed petrographic and
158 geochemical analysis (Table A3), among the four types of amphibole-bearing samples listed in
159 Table A2: (1) 8 samples with amphibole-bearing GSR zones, in which amphibole recrystallized
160 together with the primary minerals of the peridotite (Fig. 3); (2) 7 amphibole-bearing melt-
161 impregnated samples, in which amphibole recrystallized together with olivine and chlorite
162 (Fig. 4); (3) 4 amphibole mylonites (Fig. 5a-c), and (4) 9 amphibole-bearing serpentinized
163 peridotites in which amphibole replaced primary minerals in veins or in microshear zones (Fig.
164 5d-f).
165 Microstructures were studied in thin sections using both optical polarizing and scanning
166 electron microscopy (SEM). Electron backscattered images obtained by SEM were used to

characterize the fine-grained recrystallized assemblages, especially amphiboles in GSR zones that were often too small to be optically identified.

We also performed electron microprobe analysis to measure major elements concentrations of amphibole and primary minerals (olivine, orthopyroxene, clinopyroxene, spinel) using a Cameca SX-100 electron microprobe (CAMPARIS service, Paris). The acceleration voltage was fixed at 15 kV and beam current at 10 nA. The spot size was 1-2 µm. Counting time was 10 s. Representative major element compositions of amphibole are shown in Table 1. The whole dataset used for Fig. 6-9 is accessible in the supplementary material of this study (Tables A4-A6) and was partially published in Bickert et al. (2020) for pyroxenes and spinel composition, and in Bickert et al. (2021) for composition of amphiboles in GSR zones.

4. Results

4.1. Microstructures and amphibole composition in the amphibole-bearing ultramafic samples

Our first objective is to provide microstructural and chemical constraints on the nature of the fluids driving amphibole crystallization in the GSR zones (Fig. 3). For this we compare both the microstructures (Fig. 3-5) and the composition of these synkinematic amphiboles (Fig. 6a-b) with those of amphiboles present in the three other amphibole-bearing types (Fig. 6c-d, 7-8).

4.1.1. Peridotites with amphibole-bearing GSR zones

188 Peridotites with amphibole-bearing GSR zones are spinel-bearing harzburgites and
189 lherzolites. Primary mineralogy is composed of large olivine and orthopyroxene grains (up to
190 2 cm in size; Bickert et al., 2021) with various amounts of clinopyroxene and spinel grains.
191 Anastomosing zones of GSR mainly develop at contact between olivine and orthopyroxene
192 porphyroclasts (Fig. 3a, c). The neoblasts' grain size ranges from 1.5 to 84 µm (Bickert et al.,
193 2020, 2021). The mineralogy of the recrystallized assemblage varies depending on the
194 porphyroclasts at contact with: polymineralic (olivine, orthopyroxene, spinel, minor
195 clinopyroxene and amphibole) along orthopyroxene porphyroclasts (Fig. 3a-d), or nearly
196 monomineralic (olivine and minor spinel and amphibole) near olivine porphyroclasts (Fig. 3e).
197 In polymineralic GSR zones, minute amounts of colorless polygonal to prismatic amphibole
198 crystals coexist with neoblasts of olivine, orthopyroxene and spinel (Fig. 3b, d). The polygonal
199 shapes of these amphiboles indicate a textural equilibrium with the other recrystallized
200 phases (Fig. 3b, 3d). In a few samples, we also observed discordant veins of undeformed
201 prismatic amphibole crosscutting all microstructures, including the GSR zones, with sharp
202 contacts (Fig. 3e-f).
203 Compositionally, amphibole in GSR zones are mostly edenites to Mg-rich hornblendes, with
204 few tremolites (Si values: 6.32 - 7.76, $(Na+K)_A$ values: 0.1-0.7; Fig. 6a; Table 1). One sample
205 contains synkinematic pargasitic amphiboles (SMS-DR17-4-31, Si values of 6.32 – 6.51, $(Na+K)_A$
206 values of 0.3-0.7; Figs. 6a, 7a). TiO_2 content is overall low (< 0.72 wt. %), mostly < 0.5 wt. %
207 (Fig. 6b; Table A3). Mg# values range from 87.5 to 95.5 (Fig. 6b). Chlorine concentrations range
208 from below the detection limit to 0.33 wt. % (Tables 1, A4). The intra-sample variability of
209 amphibole composition spans the whole pargasite to tremolite trend (Figs 7a-b), with small
210 variations related to the minerals micro-aggregation: amphibole in olivine-rich zones have
211 more depleted alkaline and iron concentrations (close to tremolitic composition) than in

polymineralic zones (Figs. 7a-b). Amphibole from veins cutting the initial mineralogy globally follow the same trend, suggesting a similar origin as amphibole in GSR zones, despite a slight enrichment in alkali and iron (Figs. 7a-b, 7e; Table 1).

4.1.2. Amphibole-bearing, impregnated ultramafic samples

Amphibole-bearing, melt-impregnated ultramafic samples are spinel-bearing harzburgites and lherzolites with porphyroclastic textures (Table A3). Olivine is mostly preserved and weakly deformed, with undulose extinction and subgrain boundaries (Fig. 4a-b). By contrast, no orthopyroxene porphyroclasts nor melt impregnation veins are preserved in these samples; plagioclase is absent. Instead, oriented, fibrous to tabular, amphibole and bluish chlorite crystals form irregularly branched microshear zones that dissect the primary mineralogy, creating angular olivine-rich clasts (Fig. 4a-b). At contact with the amphibole and chlorite microshear zones, amphibole and olivine locally recrystallize together in polygonal grains, with a much coarser grain size than in the GSR zones (70-160 µm; Fig. 4b, d-e). Amphibole also locally crystallizes along corroded olivine grain boundaries (Fig. 4d-e). Serpentine is in every case a later alteration product, forming veins that crosscut both the olivine-rich clasts and the amphibole-chlorite domains (Fig. 4a, c).

Figure 4c shows a detail of a sample with amphibole-rich bands up to 8 mm-thick (Fig. 2c), composed of deformed, colorless oriented amphibole porphyroclasts and recrystallized amphibole grains, and defining a foliation (Fig. 4c). These amphibole-rich bands are interlayered with polymineralic domains composed of altered pyroxene porphyroclasts in a matrix of fine-grained amphibole and chlorite. Late microshear zones of deformed chlorite and serpentine enclose elongated relicts of olivine and of deformed spinel porphyroclasts, forming alteration haloes around spinels (Fig. 4c).

Compositionally, amphibole grains from amphibole-bearing melt-impregnated ultramafic samples also have pargasite to Mg-hornblende compositions, with a wider range of Si (6.35 – 7.96) and $(Na+K)_A$ values (0 – 0.93) than the amphiboles in GSR zones (Fig. 6c). Yet, they define a different trend than amphiboles in GSR zones, with higher $(Na+K)_A$ values at a given Si content (Fig. 6c). TiO_2 and Mg# contents are quite similar between the two types (< 0.57 wt. % and 86.7 – 96.6, respectively; Fig. 6d). Chlorine concentrations are overall lower than for amphibole in GSR zones (<0.17 wt. %; Tables 1, A4). As for amphibole in the GSR zones, amphibole composition varies slightly according to the nature of minerals phase at contact with, the few tremolites being located next to olivine grains (Figs. 7f-h; Table 1).

4.1.3. Amphibole mylonites

In amphibole mylonites, the initial mineralogy is totally overprinted by hydrous minerals, which makes difficult the identification of the initial protolith. Yet, the high amounts of chlorite and/or talc in the matrix (Fig. 5a, c) suggest that the protolith was a mixture of peridotite and gabbro (Albers et al., 2019; Bach et al., 2012; Boschi et al., 2006; Picazo et al; 2012). Amphibole mylonites show alternation of amphibole-rich domains with polymineralic domains (Fig. 5a-b). One sample shows a microshear zone in a large clinopyroxene grain, with recrystallization of both clinopyroxene and brown amphibole (Fig. A1). Amphibole-rich domains are mainly composed of prismatic brown amphibole porphyroclasts (Fig. 5a), while polymineralic domains are mostly composed of very small grains of amphibole, bluish to grey chlorite and talc (Fig 5a, c). Brown amphibole porphyroclasts, and former pyroxenes replaced by amphibole commonly form syntectonic rolling structures (δ- to σ-types), with pressure shadow rims composed of acicular amphibole ± chlorite ± talc (Fig. 5a, c). Spinel relicts are rare but present in several samples. Post-deformation veins of talc are common (Fig 5c).

As for the two first amphibole-bearing types, most amphiboles in these mylonites have edenitic to Mg-rich hornblende compositions (Fig. 8a-b). Yet, they differ by their high TiO_2 contents, which are mostly > 1 wt. % (0.27 - 3.64 wt.%; Fig. 8b; Table 1). Samples from the DR33 (from an exposed corrugated footwall; Cannat et al., 2006) are the most enriched in alkali and iron (Mg# < 83), while amphibole from the two other samples (DR27 and DR34) are more magnesian (Mg# of 85–94; Fig. 8b). Chlorine concentrations range from below the detection limit to 0.25 wt. % (Tables 1, A4). Amphibole composition in these mylonites also show a slight variability depending on the microstructures, with deformed amphibole porphyroclasts having higher TiO_2 and Al contents (> 1 wt.% and 1 a.p.f.u respectively), and lower Si < 7 a.p.f.u. (Fig. 8a-b and Table A3) than smaller amphiboles from polymineralic domains.

4.1.4. Amphibole-bearing serpentinized ultramafic samples

In amphibole-bearing serpentinized ultramafic samples, amphibole replaces pyroxenes (Fig. 5d-e), or occurs as fibrous crystals in late micro shear zones (Fig. 5e), or in the serpentinized groundmass (Fig. 5f; Table 1). Olivine is fully replaced, either by serpentine, or by oxide-bearing mineral assemblages (Fig. 5a). Chlorite when present postdates amphibole formation and is associated with serpentine in late microshear zones (Table A3). Serpentine products form veins that crosscut amphibole-rich domains (Fig. 5d-f).

Compositionally, amphibole in these extensively serpentinized samples is mostly tremolitic, with a few Mg-hornblendes (Fig. 8c; Table 1). Si values are mostly high (7.28-8 a.p.f.u.) with low $(Na+K)_A$ concentrations (< 0.41). All amphibole grains have low TiO_2 content (< 0.32 wt%) and Mg# shifting to higher values (94.9 - 97.8) (Fig. 8d). Chlorine concentrations do not exceed 0.13 wt. % (Tables 1; A4).

4.2. Amphibole composition and the primary mineralogy of amphibole-bearing samples

Our objective here is to identify any potential control of the protolith mineralogy on amphibole composition. For this purpose, we compare the composition of spinel and pyroxene relicts in the selected amphibole-bearing samples with existing data from the Eastern SWIR (Fig. 9; Tables A5-A6). Spinel and clinopyroxene porphyroclasts from the selected samples cover the whole compositional variations documented in peridotites from the same region by Seyler et al. (2003) and Paquet et al. (2016) (Fig. 9).

Spinel Mg# and Cr# are negatively correlated following the global trend of the abyssal peridotites (Dick and Fisher, 1984) (Fig. 9a). The four types of amphibole-bearing samples plot in different parts of the trend: amphibole mylonites have the most Cr-rich spinel (Cr# values of 42.5-43.6, Fig. 9a), also enriched in iron (Mg# <50; Fig. 9a) and in TiO_2 (> 0.15 wt%; Fig. 9b). Spinel from amphibole-bearing, melt-impregnated ultramafic samples show higher Mg# (53.6 – 61.3) at lower Cr# values (31.7-39.4; Fig. 9a). Spinel TiO_2 content is in the same range as in amphibole mylonites (Fig. 9b). Plagioclase-bearing peridotites from this region of the SWIR have similar spinel composition to these two amphibole-bearing types, consistent with a protolith resulting from chemical interactions between peridotite and a variably evolved melt (Fig. 9a-b; Paquet et al., 2016). By contrast, peridotites with amphibole-bearing GSR zones have spinel with lower Mg# and Cr# values (60.9 - 71.3 and 21.7-33.8, respectively; Fig. 9a), and with TiO_2 contents < 0.15 wt.% (Fig. 9b). The rare spinel relicts from amphibole-bearing serpentinized ultramafic samples have similar compositions, within the range of other residual peridotite samples from the eastern SWIR (amphibole-free GSR bearing samples from the *Smoothseafloor* dredges, and other samples studied by Seyler et al., 2003; Fig. 9a-b). Overall,

spinel and amphibole Mg# show a similar decreasing trend with increasing the degree of melt-impregnation (Fig. 9b, Fig. 10b, d).

Compositions of clinopyroxene porphyroclasts in samples with amphibole-bearing GSR zones covers the entire range of clinopyroxene composition recorded in other residual peridotites from the eastern SWIR, including those with amphibole-free GSR zones (Figs. 9c-d). Due to the extent of alteration, clinopyroxene composition was measured in only one amphibole-bearing melt-impregnated ultramafic sample and one amphibole mylonite. Clinopyroxene from the amphibole-bearing melt-impregnated ultramafic sample plots at the lower Cr_2O_3 (average of 0.70 wt.%), higher Al_2O_3 (7.43 wt.% on average) end of the trend defined by residual peridotites from the Eastern SWIR, and at similar Mg# values (90.2 on average; Figs. 9c-d). By contrast, clinopyroxene from the amphibole mylonite is more depleted in Al_2O_3 and Cr_2O_3 contents (3.08 wt.% and 0.29 wt.%, respectively; Fig. 9c), with lower Mg# (82.9; Fig. 9d). Clinopyroxene in amphibole-bearing serpentinized ultramafic samples were too altered to be measured. Overall, clinopyroxene TiO_2 contents decrease with increasing Mg# and Cr#, as also observed by Seyler et al. (2003; Fig. 9c-d; Table A6).

5. Discussion

The objective of this study is to better constrain the extent and the distribution of mantle hydration along axial detachments at the Eastern SWIR, below the domain affected by pervasive hydrothermal circulation and by serpentinization (Fig. 11). Because this region of the SWIR has a very low melt supply, plate divergence is mostly accommodated by slip along these detachment faults (Cannat et al., 2006; Sauter et al., 2013), which therefore represent the actual plate boundary (Fig. 11a).

The occurrence of small amounts of amphibole in GSR zones is evidence for the presence of small amounts of hydrous fluids in the root zone of these plate boundary faults at and near the BDT (Bickert et al., 2020; 2021). Microseismicity data (Chen et al., 2023) helps constrain this BDT region to depth >15 km. Compared to oceanic transform faults (OTFs), the other category of plate boundary faults at mid-oceanic ridges (Fig. 11b), axial detachment faults are both generally shorter lived (< 4 Myrs; Tani et al., 2011), and associated with continuous exhumation of deeply-derived material. These characteristics probably translate into substantial differences in the degree of deformation and hydration between the two categories of plate boundary faults.

5.1. A seawater-derived origin for fluids that percolate down to the root zone of eastern SWIRaxial detachment faults

In samples from the Eastern SWIR, amphibole is present in various mineralogical assemblages: (1) synkinematic with olivine ± orthopyroxene ± clinopyroxene + spinel in GSR zones (Fig. 3b-d); (2) with olivine and/or chlorite in impregnated ultramafic samples (Fig. 4a-b); (3) with chlorite ± talc in amphibole mylonites (Fig. 5a-c); (4) predating serpentine ± chlorite in the most serpentinized ultramafic samples (Fig. 5d-e). These observed mineralogical assemblages could indicate a relative chronology through exhumation, with increasing hydrous fluids content upward: very localized hydration in the GSR zones, at high temperatures (>800°C) at the root zone of detachments, close to the BDT; to more pervasive hydration conditions under greenschist facies conditions in the amphibole-bearing serpentinized peridotites. Serpentinization appears to postdate most amphibole-bearing microstructures in this whole suite, and preferentially affects olivine, leaving pyroxenes relicts except in the most extensively serpentinized samples, which suggest moderate temperatures

of serpentinization (T <400°C; Bach et al., 2004; Klein et al., 2009), consistent with the oxygen isotope results of Rouméjon et al. (2015).

The amphiboles in the studied suite of rocks can result from (1) magmatic infiltrations or dikes in the peridotite (Cannat & Seyler, 1995; Cipriani et al., 2009; Schroeder & John, 2004); (2) sea-water, suggesting deep percolation of hydrothermal fluids in the mantle lithosphere, down to the root of the fault at the BDT (Cannat & Seyler, 1995; Kohli & Warren, 2020; Prigent et al., 2020; Vieira Duarte et al., 2020); or (3) crystallizing from small amounts of water in the residual lherzolitic mantle (Alard et al., 2022; Le Roux et al., 2021; Schmädicke et al., 2018).

It is unlikely that the amphibole in GSR zones crystallized from hydrous fluids trapped in mantle primary minerals. Water dissolved in residual mantle paragenesis would be close to or lower than the average mantle source, i.e. circa 200 ppm in olivine (Urann et al., 2017), which is a too low amount to the formation of monomineralic amphibole veins crosscutting the microstructures (Fig. 3e-f), with similar composition as those in GSR zones (Fig. 7a-e).

Then, if amphiboles have a purely magmatic origin, they would be expected to have a pargasitic composition with high Fe, Ti and Na content, as described for amphiboles in samples from the MAR (Fig. 10a-b; Albers et al., 2019; Picazo et al., 2012). This is the case for some amphibole in the amphibole mylonites, in which Ti-rich brown amphibole porphyroclasts (Fig. 5c, 8b) have compositions close to those in amphibole-bearing samples from the MAR at 15°N (Fig. 10a-b) and from SWIR gabbros (Dick et al., 2002; Ozawa et al., 1991; Paquet et al., 2016). Yet, in the same samples, the subsequent replacement of primary minerals, including the Ti-rich amphiboles, coupled with the evolution of the mineralogical assemblage (tremolitic to edenitic amphibole + chlorite + talc) also indicate a hydrous fluid-dominated alteration regime, under greenschist conditions (Jöns et al., 2010; Klein et al., 2015), which is in favor of a hydrothermal fluid circulation.

379 Amphibole from GSR zones have edenitic to Mg-hornblende compositions, with low TiO_2
380 content (<1wt. %; Fig. 6b). These compositions are closer to those of amphibole interpreted
381 as derived from seawater percolation in peridotites from OTFs (Fig. 10c-d). In addition, the
382 similarity of amphibole composition in GSR zones and in the other amphibole-bearing types,
383 that are of more clear hydrothermal origin, point to a common hydrothermal origin (Fig. 10).
384 The initial mineralogical assemblage of Olivine + Orthopyroxene ± Clinopyroxene + Cr-rich
385 spinel, typical of residual peridotites (Fig. 9), is also consistent with simple hydration of
386 peridotites, at temperatures > 650°C, which would lead to a transition from granulite to
387 amphibolite facies, in which pyroxenes are consumed to form amphibole (Cipriani et al., 2009;
388 Spear, 1981; Vieira Duarte et al., 2020). Amphibole crystals in GSR zones and to a lesser extent
389 in melt-impregnated ultramafic samples are indeed in textural equilibrium with primary
390 minerals (olivine, orthopyroxene, spinel; Fig. 3b, d; 4b). However, the low abundance of
391 amphibole in GSR zones, the highly localized distribution of hydrous minerals along zones of
392 high strength contrasts such as orthopyroxene boundaries and GSR zones (Fig. 3a-c; 4c-d),
393 coupled with the incomplete replacement of primary minerals, suggest that hydration was
394 very limited.
395 Limited hydration in amphibole-bearing GSR zones and in the melt-impregnated
396 ultramafic samples is consistent with the intrasample variability of amphibole composition
397 driven by the minerals in contact (Fig. 7).(Fig. 7), suggests that fluid composition was buffered
398 by the protolith. This variability, and the strict localization of hydrous minerals along high
399 strength zones, point to a rock-dominated hydration at low water-rock ratios. We thus
400 propose that local fluid composition, and the resulting amphibole composition were buffered
401 by the protolith: lherzolites to harzburgites for amphibole in the GSR zones; and mixture of
402 residual peridotite and gabbroic impregnations and dikelets for amphibole in melt-

403 impregnated samples. The latter have similar microstructures, alkaline contents and spinel
404 iron enrichment to hydrothermally altered melt-impregnated peridotites from the MAR (Fig.
405 10a, c; Albers et al., 2019; Jöns et al., 2010; Picazo et al., 2012). The correlation between spinel
406 Mg# and amphibole Mg# for the four amphibole-bearing types, with varying degrees of melt-
407 impregnation (Figs. 9b, 10b), is consistent with fluid composition being buffered by the
408 protolith, as variably melt-impregnated domains are then replaced by amphibole (Figs. 4-5).
409 Therefore, amphibole composition, deriving from primary minerals, would reflect the
410 processes that have affected the protolith itself, such as the interaction of more or less
411 evolved melts with the host peridotite, at high temperature (Paquet et al., 2016).
412
413 **5.2. Detachment-related deformation and bidirectional fluid flow**
414 Microstructural and compositional observations in amphibole-bearing SWIR samples
415 allow to reconstruct deep fluid flow along axial detachment faults in a magma-poor plate
416 divergence context (Fig. 11a). At depth, brittle fracture and shear zones forming the
417 detachment grade into a system of anastomosing, crystal plastic to semi-brittle shear zones
418 (Fig. 11a, c; Bickert et al., 2021). This moving anastomosed network allows the exhumation of
419 rocks deformed in high strain zones at relative high P-T conditions to shallower depths and
420 pressures. On the one hand, these microfractures act as fluid pathways for small amounts of
421 seawater-derived fluids that percolate down to the BDT domain. In addition to brittle
422 microstructures, mineral scale heterogeneity, such as between brittle orthopyroxene and
423 dominantly plastic olivine, can create small-scale stress concentrations that will help localize
424 strain, favoring fluid circulation and further focusing deformation (Bickert et al., 2021; Dygert
425 et al., 2019; Ismail et al., 2021; Lopez-Sanchez et al., 2021).

On the other hand, magmatic fluids episodically move up along the deformation system (Fig. 11c), resulting in the melt-impregnated and gabbro injected ultramafic samples described by Paquet et al. (2016). In amphibole-bearing melt-impregnated ultramafic samples, the olivine-rich clasts (Fig. 4a-c) may have resulted from local melt injections, as the peridotite entered into the brittle part of the axial lithosphere (Fig. 11c; Albers et al., 2019; Picazo et al., 2012). The syn-recrystallization of olivine and amphibole neoblasts (Fig. 4a-b, d-e), nonetheless suggests that hydration of these gabbroic dikelets started during the late stages of the high stress semi-brittle deformation affecting primary minerals, at temperatures <750°C (Fumagalli et al., 2005). It is worth noting that no massive gabbroic sequences were recovered at the Eastern SWIR, but rather small dikelets or parts of dikes in contact with peridotites (Paquet et al., 2016). This is in accordance with the very low magma budget of this region of the SWIR and differs from other slow and ultraslow locations where large gabbroic bodies, with extensive ductile strain have been drilled in detachments footwalls (Cannat, 1991; Hansen et al., 2013).

As the rock material is exhumed into shallower depths, hydration becomes more pervasive, eventually switching from a rock-dominated to a fluid-dominated alteration regime (Fig. 11d). Samples altered under greenschist facies conditions, such as amphibole-bearing ultramafic samples and mylonites, show higher proportions of low temperature hydrous minerals that are not only focused along zones of high strength contrasts, but also occur in the groundmass (Fig. 5d-f). As exhumation proceeds, significant shear stresses affect the detachment but also its footwall (Lavier et al., 1999; Sandiford et al., 2021). Rouméjon et al. (2014) proposed that initial microfracturing, providing pathways for hydrous fluids and leading to the serpentinization mesh texture, form in response to tectonic stresses combined with peridotite cooling from 800°C to 400°C. The generation of an interconnected porosity through

more pervasive cracking, in part due to serpentinization-induced volume change, would characterize the hydrothermal domain. In this domain, the alteration of magmatic minerals and of gabbro-infiltrated peridotite into chlorite- and talc-bearing assemblages, which are weaker than serpentine, locally facilitates strain localization (Boschi et al., 2006; Escartín et al., 2003; Picazo et al., 2012; Schroeder and John, 2004).

5.3. Implications for deep fluid percolation along oceanic plate boundaries

Mg-rich hornblende amphiboles similar to those described here have been observed in ultramafic samples from other magma-starved ridges, active or fossil (Boschi et al., 2006; Cannat et al., 2009; Escartín et al., 2003; Patterson et al., 2021; Picazo et al., 2012; Schroeder and John, 2004; Vieira Duarte et al., 2020), but also along active transform faults such as Shaka and Vema (Cipriani et al., 2009; Kohli et al., 2019; Prigent et al., 2020; Fig. 10c-d). In both contexts, they have been interpreted as resulting from interaction of mantle-derived rocks with limited quantities of seawater-derived fluids that percolated down to the BDT zone (i.e. the root zone of the faults), promoting fluid-assisted deformation (Prigent et al., 2020; Vieira Duarte et al., 2020, Cipriani et al., 2009). This fluid-assisted deformation combines brittle and ductile deformation mechanisms, with similar mineralogical assemblages and temperature conditions as presented here for Eastern SWIR samples (Fig. 11b; Kakihata et al., 2022; Kohli & Warren, 2020; Prigent et al., 2020).

A deep BDT is supported by recent microseismic studies that recorded hypocenters down to 15-20 km below seafloor at the Eastern SWIR (Chen et al., 2023; Grevemeyer et al., 2019; Schlindwein and Schmid, 2016), at Gakkel ridge (Meier et al., 2021; Schlindwein et al., 2015) and along OTFs (de Melo et al., 2020; Grevemeyer et al., 2021).

The similarities between the nearly amagmatic SWIR axial detachments and OTFs are therefore striking. Both are large trans-lithospheric faults acting as plate boundaries along slow or ultraslow mid-oceanic ridges. However, detachment faults systematically accommodate exhumation, while OTFs only do it under conditions of incipient extension or compression: for example transtension near ridge/transform intersections (Prigent et al., 2020; Kohli et al., 2019), or transpression forming push-up ridges such as St Paul or Romanche OTFs (Bonatti et al., 1994; Maia et al., 2016). Both the degrees of finite deformation and the intensity of fluid-assisted deformation are more extreme in OTF ultramafic samples compared with samples from the Eastern SWIR. Most OTF samples are high temperature mylonites with generalized GSR and high proportions of hydrous minerals (Cannat et al., 1990; Cipriani et al., 2009; Jaroslow et al., 1996; Kakihata et al., 2022; Kohli & Warren, 2020; Prigent et al., 2020). By contrast, the deformation recorded in peridotites in the footwall of eastern SWIR detachments is strongly heterogeneous; GSR is local, at grain scale, and observed in only 31% of the dredged ultramafic samples (Table A2). The small proportion of synkinematic amphiboles in GSR zones also indicates a very limited role for fluid-assisted deformation.

These differences in deformation intensity and hydration reflect the contrasting lifetime of both structures: axial detachment faults at the Eastern SWIR have maximum offsets of 20 km and fault activity durations are < 3 Myr (Cannat et al., 2019). By contrast, OTFs are long-lived strike-slip faults with offsets reaching several hundreds of kilometers (Grevemeyer et al., 2021; Ligi et al., 2002). The maturity of OTFs allows long-lived strain accumulation in the mantle material, and a long-lasting exposure to seawater-derived fluids that percolate down to BDT level.

At the Eastern SWIR, strain accumulation is limited by the short lifetime of detachment faults (Cannat et al., 2019), and by the fact that mantle rocks are continuously exhumed out

of the BDT into higher structural levels: the vertical exhumation along detachment faults implies a steady renewal of the lithospheric mantle involved in deformation and hydration. Fractures and microshear zones composing the detachment in the BDT zone allow fluid circulation (Fig. 11c-d);The fractured BDT material is then exhumed to shallower structural domains and new fractures and microfractures need to be formed in the newly, freshly exhuming BDT mantle. We propose that this constant regeneration of the mantle material along the detachment would limit pervasive fluid penetration and strain accumulation into the deep axial lithosphere.

6. Conclusions

At the Eastern SWIR, detachment faults exhume variably serpentinized ultramafic rocks on the seafloor. A third of these samples investigated as part of this work show evidence of fluid circulation beyond the serpentine stability field, by the occurrence of high-temperature Mg-hornblende to tremolitic deformed amphibole crystals. The composition of these amphiboles favors a hydrothermal origin. Seawater-derived fluids circulate along fractures and microfractures composing the axial detachment, down to the root zone of the fault, at the BDT zone. Fluid circulation is controlled by both brittle microfractures and small-scale rheological contrasts that focus fluids and along which amphibole forms preferentially. Amphibole composition is also controlled by the composition of the initial protolith. The extent and the distribution of mantle hydration along detachments from the Eastern SWIR is similar to those observed along oceanic transform faults, despite much smaller intensity. We propose that the vertical exhumation of new material along the detachment fault coupled with the shorter lifetime of these detachments compared to OTFs, prevent a more pervasive deformation and hydration.

Data Avaibility

Microprobe data on which the results of this work are based are available on the Supplementary material of this study.

Acknowledgements

The authors thank Nick Dygert, an anonymous reviewer and the guest editor Frieder Klein for their helpful comments and suggestions. Partial funding of this work was supported by PRIN 2017 (PRIN2017KY5ZX8) and by ANR project «Ridge-Factory-Slow » (ANR- 18-CE01-0002). Thanks to the IPGP Marine Rock Repository for sample curation. The authors are grateful to M. Quintin for providing the thin sections, to M. Fialin and N. Rividi for their technical assistance at the CAMPARIS service in Paris. The IPGP SEM facility is supported by the IPGP multidisciplinary program PARI, and by Region île-de-France SESAME Grant no. 12015908.

Appendix A - Supplementary material

In this section we provide tables of data and additional figures that give further support for the results we presented in the paper. Table A1 displays the depths and positions of the dredges of *Smoothseafloor* cruise (https://doi.org/10.17600/10200050) and of the in-situ sample from *Rovsmooth* cruise (https://doi.org/10.17600/16002000). Table A2 classifies the different types of amphibole-bearing ultramafic samples and their relative estimated abundances. Table A3 provides the IGSN codes and the microstructural characteristics of the 28 samples analyzed in this study. Tables A4 to A6 respectively provide microprobe data

543 measured on amphibole, clinopyroxene and spinel from the selected amphibole-bearing
544 ultramafic samples.
545 Figure A1 shows prehnite grains in amphibole mylonites, as a hint for a magmatic protolith.
546

547 ## References

548 Alard, O., Halimulati, A., Demouchy, S., 2022. Look between the grains. Nat. Geosci. 15, 856–
549 857. https://doi.org/10.1038/s41561-022-01065-3
550 Albers, E., Schroeder, T., Bach, W., 2019. Melt Impregnation of Mantle Peridotite Facilitates
551 High-Temperature Hydration and Mechanical Weakening: Implications for Oceanic
552 Detachment Faults. Geochemistry, Geophys. Geosystems 20, 84–108.
553 https://doi.org/10.1029/2018GC007783
554 Bach, W., Garrido, C.J., Paulick, H., Harvey, J., Rosner, M., 2004. Seawater-peridotite
555 interactions: First insights from ODP Leg 209, MAR 15°N. Geochemistry, Geophys.
556 Geosystems 5. https://doi.org/10.1029/2004GC000744
557 Bach, W., Jons, N., Klein, F., 2012. Metasomatism Within the Ocean Crust, in: Transformation
558 of Rock. https://doi.org/10.1007/978-3-642-28394-9
559 Bickert, M., Cannat, M., Tommasi, A., Jammes, S., Lavier, L., 2021. Strain Localization in the
560 Root of Detachment Faults at a Melt-Starved Mid-Ocean Ridge : A Microstructural Study
561 of Abyssal Peridotites From the Southwest Indian Ridge. Geochemistry, Geophys.
562 Geosystems 22, 1–29. https://doi.org/10.1029/2020GC009434
563 Bonatti, E., Ligi, M., Gasperini, L., Peyve, A., Raznitsin, Y., Chen, Y.J., 1994. Transform migration
564 and vertical tectonics at the Romanche Fracture Zone, equatorial Atlantic. J. Geophys.
565 Res. 99. https://doi.org/10.1029/94jb01178
566 Boschi, C., Früh-Green, G.L., Delacour, A., Karson, J.A., Kelley, D.S., 2006. Mass transfer and

567 fluid flow during detachment faulting and development of an oceanic core complex,
568 Atlantis Massif (MAR 30°N). Geochemistry, Geophys. Geosystems 7.
569 https://doi.org/10.1029/2005GC001074
570 Brunelli, D., Sanfilippo, A., Bonatti, E., Skolotnev, S., Escartin, J., Ligi, M., Ballabio, G., Cipriani,
571 A., 2020. Origin of oceanic ferrodiorites by injection of nelsonitic melts in gabbros at the
572 Vema Lithospheric Section, Mid Atlantic Ridge. Lithos 368–369, 105589.
573 https://doi.org/10.1016/j.lithos.2020.105589
574 Cann, J.R., Blackman, D.K., Smith, D.K., McAllister, E., Janssen, B., Mello, S., Avgerinos, E.,
575 Pascoe, A.R., Escartin, J., 1997. Corrugated slip surfaces formed at ridge-transform
576 intersections on the Mid-Atlantic Ridge. Nature 385, 329–332.
577 https://doi.org/10.1038/385329a0
578 Cannat, M., 1993. Emplacement of Mantle Rocks in the Seafloor. J. Geophys. Res. 98, 4163–
579 4172.
580 Cannat, M., Juteau, T., Berger, E., 1990. 5. PETROSTRUCTURAL ANALYSIS OF THE LEG 109
581 SERPENTINIZED PERIDOTITES. Proc. Ocean Drill. Program, Sci. Results, Vol. 106/109 106,
582 47–56.
583 Cannat, M., Sauter, D., Escartín, J., Lavier, L., Picazo, S., 2009. Oceanic corrugated surfaces and
584 the strength of the axial lithosphere at slow spreading ridges. Earth Planet. Sci. Lett.
585 https://doi.org/10.1016/j.epsl.2009.09.020
586 Cannat, M., Sauter, D., Lavier, L., Bickert, M., Momoh, E., Leroy, S., 2019. On spreading modes
587 and magma supply at slow and ultraslow mid-ocean ridges. Earth Planet. Sci. Lett. 519,
588 223–233. https://doi.org/10.1016/j.epsl.2019.05.012
589 Cannat, M., Sauter, D., Mendel, V., Ruellan, E., Okino, K., Escartin, J., Combier, V., Baala, M.,
590 2006. Modes of seafloor generation at a melt-poor ultraslow-spreading ridge. Geology

591 34, 605–608. https://doi.org/10.1130/G22486.1
592 Cannat, M., Sauter, D., Rouméjon, S., 2012. Formation of an ultramafic seafloor at the
593 Southwest Indian Ridge 62°-65°E : internal structure of detachment faults and sparse
594 volcanism documented by sidescan sonar and dredges, AGU Fall Meeting Abstracts.
595 Cannat, M., Seyler, M., 1995. Transform tectonics, metamorphic plagioclase and
596 amphibolitization in ultramafic rocks of the Vema transform fault (Atlantic Ocean). Earth
597 Planet. Sci. Lett. 133, 283–298. https://doi.org/10.1016/0012-821X(95)00078-Q
598 Ceuleneer, G., Cannat, M., 1997. 2. High-Temperature Ductile Deformation of Site 920
599 Peridotites. Proc. Ocean Drill. Program, Sci. Results 153, 23–34.
600 https://doi.org/10.2973/odp.proc.sr.153.002.1997
601 Chen, J., Crawford, W., Cannat, M., 2023. Microseismicity and lithosphere thickness at a nearly
602 amagmatic mid-ocean ridge. PREP.
603 Cipriani, A., Bonatti, E., Seyler, M., Brueckner, H.K., Brunelli, D., Dallai, L., Hemming, S.R., Ligi,
604 M., Ottolini, L., Turrin, B.D., 2009. A 19 to 17 Ma amagmatic extension event at the Mid-
605 Atlantic Ridge: Ultramafic mylonites from the Vema Lithospheric Section. Geochemistry,
606 Geophys. Geosystems 10. https://doi.org/10.1029/2009GC002534
607 de Martin, B.J., Hirth, G., Evans, B., 2004. Experimental Constraints on Thermal Cracking of
608 Peridotite at Oceanic Spreading Centers, in: Mid-Ocean Ridges: Hydrothermal
609 Interactions Between the Lithosphere and Oceans.
610 de Melo, G.W.S., Parnell-Turner, R., Dziak, R.P., Smith, D.K., Maia, M., do Nascimento, A.F.,
611 Royer, J.-Y., 2020. Uppermost Mantle Velocity beneath the Mid-Atlantic Ridge and
612 Transform Faults in the Equatorial Atlantic Ocean. Bull. Seismol. Soc. Am.
613 https://doi.org/10.1785/0120200248
614 deMartin, B.J., Sohn, R.A., Pablo Canales, J., Humphris, S.E., 2007. Kinematics and geometry

615 of active detachment faulting beneath the Trans-Atlantic Geotraverse (TAG)
616 hydrothermal field on the Mid-Atlantic Ridge. Geology 35, 711.
617 https://doi.org/10.1130/G23718A.1
618 Dick, H.J.B., Fisher, R.L., 1984. Mineralogic Studies of the Residues of Mantle Melting: Abyssal
619 and Alpine-Type Peridotites, in: Kimberlites II: The Mantle and Crust-Mantle
620 Relationships. pp. 295–308. https://doi.org/10.1016/B978-0-444-42274-3.50031-7
621 Dick, H.J.B., Ozawa, K., Meyer, P.S., Niu, Y., Robinson, P.T., Constantin, M., Hebert, R., Maeda,
622 J., Natland, J., Hirth, G., Mackie, S.M., 2002. Primary silicate mineral chemistry of a 1.5-
623 km section of very slow spreading lower ocean crust: ODP Hole 735B, Southwest Indian
624 Ridge. Proc. Ocean Drill. Program, 176 Sci. Results.
625 https://doi.org/10.2973/odp.proc.sr.176.001.2002
626 Dygert, N., Bernard, R.E., Behr, W.M., 2019. Great Basin Mantle Xenoliths Record Active
627 Lithospheric Downwelling Beneath Central Nevada. Geochemistry, Geophys. Geosystems
628 20, 751–772. https://doi.org/10.1029/2018GC007834
629 Escartín, J., Andreani, M., Hirth, G., Evans, B., 2008. Relationships between the microstructural
630 evolution and the rheology of talc at elevated pressures and temperatures. Earth Planet.
631 Sci. Lett. 268, 463–475. https://doi.org/10.1016/j.epsl.2008.02.004
632 Escartin, J., Hirth, G., Evans, B., 1997. Effects of serpentinization on the litshopheric strength
633 and the style of normal faulting at slow-spreading ridges. Earth Planet. Sci. Lett. 151, 181–
634 189.
635 Escartín, J., Mével, C., MacLeod, C.J., McCaig, A.M., 2003. Constraints on deformation
636 conditions and the origin of oceanic detachments: The Mid-Atlantic Ridge core complex
637 at 15°45'N. Geochemistry, Geophys. Geosystems 4, 1–37.
638 https://doi.org/10.1029/2002GC000472

639 Escartín, J., Mével, C., Petersen, S., Bonnemains, D., Cannat, M., Andreani, M., Augustin, N.,
640 Bezos, A., Chavagnac, V., Choi, Y., Godard, M., Haaga, K., Hamelin, C., Ildefonse, B.,
641 Jamieson, J., John, B., Leleu, T., MacLeod, C.J., Massot-Campos, M., Nomikou, P., Olive,
642 J.A., Paquet, M., Rommevaux, C., Rothenbeck, M., Steinfuhrer, A., Tominaga, M., Triebe,
643 L., Campos, R., Gracias, N., Garcia, R., 2017. Tectonic structure, evolution, and the nature
644 of oceanic core complexes and their detachment fault zones (13°20'N and 13°30'N, Mid
645 Atlantic Ridge). Geochemistry, Geophys. Geosystems 18, 1451–1482.
646 https://doi.org/10.1002/2016GC006775
647 Fruh-green, G.L., Connolly, J.A.D., Plas, A., Kelley, D.S., Grobety, B., 2004. Serpentinization of
648 Oceanic Peridotites : Implications for Geochemical Cycles and Biological Activity The
649 Subseafloor Biosphere at Mid-Ocean Ridges. Geophys. Monogr. Ser. 144, 119–136.
650 Fumagalli, P., Zanchetta, S., Poli, S., 2009. Alkali in phlogopite and amphibole and their effects
651 on phase relations in metasomatized peridotites: A high-pressure study. Contrib. to
652 Mineral. Petrol. 158, 723–737. https://doi.org/10.1007/s00410-009-0407-4
653 Grevemeyer, I., Hayman, N.W., Lange, D., Peirce, C., Papenberg, C., Van Avendonk, H.J.A.,
654 Schmid, F., de La Peña, L.G., Dannowski, A., 2019. Constraining the maximum depth of
655 brittle deformation at slow- and ultraslow-spreading ridges using microseismicity.
656 Geology 47, 1069–1073. https://doi.org/10.1130/g46577.1
657 Grevemeyer, I., Rüpke, L.H., Morgan, J.P., Iyer, K., Devey, C.W., 2021. Extensional tectonics
658 and two-stage crustal accretion at oceanic transform faults. Nature 591, 402–407.
659 https://doi.org/10.1038/s41586-021-03278-9
660 Harigane, Y., Abe, N., Michibayashi, K., Kimura, J.-I., Chang, Q., 2016. Melt-rock interactions
661 and fabric development of peridotites from North Pond in the Kane area, Mid-Atlantic
662 Ridge: Implications of microstructural and petrological analyses of peridotite samples

663 from IODP Hole U1382A. Geochemistry Geophys. Geosystems 17, 2298–2322.
664 https://doi.org/10.1002/2016GC006429.
665 Ismail, W. Ben, Tommasi, A., Lopez-Sanchez, M.A., Rutter, E.H., Barou, F., Demouchy, S., 2021.
666 Deformation of upper mantle rocks with contrasting initial fabrics in axial extension.
667 Tectonophysics 815. https://doi.org/10.1016/j.tecto.2021.228997
668 Jaroslow, G.E., Hirth, G., Dick, H.J.B., 1996. Abyssal peridotite mylonites: implications for grain-
669 size sensitive flow and strain localization in the oceanic lithosphere. Tectonophysics 256,
670 17–37. https://doi.org/10.1016/0040-1951(95)00163-8
671 Jöns, N., Bach, W., Klein, F., 2010. Magmatic influence on reaction paths and element
672 transport during serpentinization. Chem. Geol. 274, 196–211.
673 https://doi.org/10.1016/j.chemgeo.2010.04.009
674 Kakihata, Y., Michibayashi, K., Dick, H.J.B., 2022. Heterogeneity in texture and crystal fabric of
675 intensely hydrated ultramylonitic peridotites along a transform fault, Southwest Indian
676 Ridge. Tectonophysics 823, 229206. https://doi.org/10.1016/j.tecto.2021.229206
677 Karato, S.-I., Paterson, M.S., Fitzgerald, J.D., 1986. Rheology of Synthetic Olivine Aggregates:
678 Influence of Grain Size and Water. J. Geophys. Res. 91, 8151–8176.
679 https://doi.org/10.1029/JB091iB08p08151
680 Klein, F., Bach, W., Jöns, N., McCollom, T., Moskowitz, B., Berquó, T., 2009. Iron partitioning
681 and hydrogen generation during serpentinization of abyssal peridotites from 15°N on the
682 Mid-Atlantic Ridge. Geochim. Cosmochim. Acta 73, 6868–6893.
683 https://doi.org/10.1016/j.gca.2009.08.021
684 Klein, F., Grozeva, N.G., Seewald, J.S., McCollom, T.M., Humphris, S.E., Moskowitz, B., Berquó,
685 T.S., Kahl, W.A., 2015. Fluids in the Crust. Experimental constraints on fluid-rock reactions
686 during incipient serpentinization of harzburgite. Am. Mineral. 100, 991–1002.

https://doi.org/10.2138/am-2015-5112

Kohli, A., Wolfson-Schwehr, M., Prigent, C., Warren, J.M., 2021. Oceanic transform fault seismicity and slip mode influenced by seawater infiltration. Nat. Geosci. 14, 606–611. https://doi.org/10.1038/s41561-021-00778-1

Kohli, A.H., Warren, J.M., 2020. Evidence for a Deep Hydrologic Cycle on Oceanic Transform Faults. J. Geophys. Res. Solid Earth 125, 1–23. https://doi.org/10.1029/2019JB017751

Le Roux, V., Urann, B.M., Brunelli, D., Bonatti, E., Cipriani, A., Demouchy, S., Monteleone, B.D., 2021. Postmelting hydrogen enrichment in the oceanic lithosphere. Sci. Adv. 7, 1–11. https://doi.org/10.1126/sciadv.abf6071

Ligi, M., Bonatti, E., Gasperini, L., Poliakov, A.N.B., 2002. Oceanic broad multifault transform plate boundaries. Geology 30, 11–14. https://doi.org/10.1130/0091-7613(2002)030<0011:OBMTPB>2.0.CO;2

Lopez-Sanchez, M.A., Tommasi, A., Ismail, W. Ben, Barou, F., 2021. Dynamic recrystallization by subgrain rotation in olivine revealed by electron backscatter diffraction. Tectonophysics 815, 228916. https://doi.org/10.1016/j.tecto.2021.228916

MacLeod, C.J., Escartin, J., Banerji, D., Banks, G.J., Gleeson, M., Irving, D.H.B., Lilly, R.M., McCaig, A.M., Niu, Y., Allerton, S., Smith, D.K., 2002. Direct geological evidence for oceanic detachment faulting: The Mid-Atlantic Ridge, 15 45N. Geology 30, 879–882. https://doi.org/10.1130/0091-7613(2002)030<0879:DGEFOD>2.0.CO;2

Maia, M., Sichel, S., Briais, A., Brunelli, D., Ligi, M., Ferreira, N., Campos, T., Mougel, B., Brehme, I., Hémond, C., Motoki, A., Moura, D., Scalabrin, C., Pessanha, I., Alves, E., Ayres, A., Oliveira, P., 2016. Extreme mantle uplift and exhumation along a transpressive transform fault. Nat. Geosci. 9, 619–623. https://doi.org/10.1038/ngeo2759

Meier, M., Schlindwein, V., Scholz, J., Geils, J., Schmidt-Aursch, M.C., Krüger, F., Czuba, W.,

711 Janik, T., 2021. Segment-Scale Seismicity of the Ultraslow Spreading Knipovich Ridge.
712 Geochemistry, Geophys. Geosystems 22. https://doi.org/10.1029/2020GC009375
713 Ozawa, K., Meyer, P.S., Bloomer, S.H., 1991. Mineralogy and Textures of Iron-Titanium Oxide
714 Gabbros and Associated Olivine Gabbros from Hole 735B, in: Proceedings of the Ocean
715 Drilling Program, 118 Scientific Results. Ocean Drilling Program.
716 https://doi.org/10.2973/odp.proc.sr.118.125.1991
717 Paquet, M., Cannat, M., Brunelli, D., Hamelin, C., Humler, E., 2016. Effect of melt/mantle
718 interactions on MORB chemistry at the easternmost Southwest Indian Ridge (61-67°E).
719 Geochemistry Geophys. Geosystems 17, 1312–1338.
720 https://doi.org/10.1002/2015GC006205.Received
721 Parnell-Turner, R., Sohn, R.A., Peirce, C., Reston, T.J., Macleod, C.J., Searle, R.C., Simão, N.,
722 2020. Seismicity trends and detachment fault structure at 13°N, Mid-Atlantic Ridge.
723 Geology. https://doi.org/10.1130/G48420.1
724 Parnell-Turner, R., Sohn, R.A., Peirce, C., Reston, T.J., MacLeod, C.J., Searle, R.C., Simão, N.M.,
725 2017. Oceanic detachment faults generate compression in extension. Geology 45, 923–
726 926. https://doi.org/10.1130/G39232.1
727 Patterson, S.N., Lynn, K.J., Prigent, C., Warren, J.M., 2021. High temperature hydrothermal
728 alteration and amphibole formation in Gakkel Ridge abyssal peridotites. Lithos 392–393,
729 106107. https://doi.org/10.1016/j.lithos.2021.106107
730 Picazo, S., Cannat, M., Delacour, A., Escartín, J., Rouméjon, S., Silantyev, S., 2012. Deformation
731 associated with the denudation of mantle-derived rocks at the Mid-Atlantic Ridge 13°-
732 15°N: The role of magmatic injections and hydrothermal alteration. Geochemistry,
733 Geophys. Geosystems 13. https://doi.org/10.1029/2012GC004121
734 Prigent, C., Warren, J.M., Kohli, A.H., Teyssier, C., 2020. Fracture-mediated deep seawater

735 flow and mantle hydration on oceanic transform faults. Earth Planet. Sci. Lett. 532,
736 115988. https://doi.org/10.1016/j.epsl.2019.115988
737 Reston, T., 2018. Flipping detachments: The kinematics of ultraslow spreading ridges. Earth
738 Planet. Sci. Lett. 503, 144–157. https://doi.org/10.1016/j.epsl.2018.09.032
739 Reston, T.J., McDermott, K.G., 2011. Successive detachment faults and mantle unroofing at
740 magma-poor rifted margins. Geology 39, 1071–1074. https://doi.org/10.1130/G32428.1
741 Rouméjon, S., Cannat, M., 2014. Serpentinization of mantle-derived peridotites at mid-ocean
742 ridges: Mesh texture development in the context of tectonic exhumation. Geochemistry,
743 Geophys. Geosystems 15, 2354–2379. https://doi.org/10.1002/2013GC005148
744 Rouméjon, S., Cannat, M., Agrinier, P., Godard, M., Andreani, M., 2015. Serpentinization and
745 fluid pathways in tectonically exhumed peridotites from the southwest Indian ridge (62-
746 65°E). J. Petrol. 56, 703–734. https://doi.org/10.1093/petrology/egv014
747 Sauter, D., Cannat, M., Rouméjon, S., Andreani, M., Birot, D., Bronner, A., Brunelli, D., Carlut,
748 J., Delacour, A., Guyader, V., MacLeod, C.J., Manatschal, G., Mendel, V., Ménez, B., Pasini,
749 V., Ruellan, E., Searle, R., 2013. Continuous exhumation of mantle-derived rocks at the
750 Southwest Indian Ridge for 11 million years. Nat. Geosci. 6, 314–320.
751 https://doi.org/10.1038/ngeo1771
752 Schlindwein, V., Demuth, A., Korger, E., Läderach, C., Schmid, F., 2015. Seismicity of the Arctic
753 mid-ocean Ridge system. Polar Sci. 9, 146–157.
754 https://doi.org/10.1016/j.polar.2014.10.001
755 Schlindwein, V., Schmid, F., 2016. Mid-ocean-ridge seismicity reveals extreme types of ocean
756 lithosphere. Nature 535, 276–279. https://doi.org/10.1038/nature18277
757 Schmädicke, E., Gose, J., Stalder, R., 2018. Water in Abyssal Peridotite: Why Are Melt-Depleted
758 Rocks so Water Rich? Geochemistry, Geophys. Geosystems 19, 1824–1843.

759 https://doi.org/10.1029/2017GC007390
760 Schroeder, T., John, B.E., 2004. Strain localization on an oceanic detachment fault system,
761 Atlantis Massif, 30°N, Mid-Atlantic Ridge. Geochemistry, Geophys. Geosystems 5.
762 https://doi.org/10.1029/2004GC000728
763 Seyler, M., Cannat, M., Mé vel, C., 2003. Evidence for major-element heterogeneity in the
764 mantle source of abyssal peridotites from the Southwest Indian Ridge (52° to 68°E).
765 Geochemistry, Geophys. Geosystems 4. https://doi.org/10.1029/2002GC000305
766 Seyler, M., Lorand, J.P., Dick, H.J.B., Drouin, M., 2007. Pervasive melt percolation reactions in
767 ultra-depleted refractory harzburgites at the Mid-Atlantic Ridge, 15° 20'N: ODP Hole
768 1274A. Contrib. to Mineral. Petrol. 153, 303–319. https://doi.org/10.1007/s00410-006-
769 0148-6
770 Smith, D.K., Cann, J.R., Escartín, J., 2006. Widespread active detachment faulting and core
771 complex formation near 13°N on the Mid-Atlantic Ridge. Nature 442, 440–443.
772 https://doi.org/10.1038/nature04950
773 Spear, F.S., 1981. An experimental study of hornblende stability and compositional variability
774 in amphibolite. Am. J. Sci. 281, 697–734.
775 Tani, K., Dunkley, D.J., Ohara, Y., 2011. Termination of backarc spreading: Zircon dating of a
776 giant oceanic core complex. Geology 39, 47–50. https://doi.org/10.1130/G31322.1
777 Tucholke, B.E., Behn, M.D., Buck, W.R., Lin, J., 2008. Role of melt supply in oceanic detachment
778 faulting and formation of megamullions. Geology 36, 455–458.
779 https://doi.org/10.1130/G24639A.1
780 Urann, B.M., Le Roux, V., Hammond, K., Marschall, H.R., Lee, C.T.A., Monteleone, B.D., 2017.
781 Fluorine and chlorine in mantle minerals and the halogen budget of the Earth's mantle.
782 Contrib. to Mineral. Petrol. 172. https://doi.org/10.1007/s00410-017-1368-7

Vieira Duarte, J.F., Kaczmarek, M.A., Vonlanthen, P., Putlitz, B., Müntener, O., 2020. Hydration of a Mantle Shear Zone Beyond Serpentine Stability: A Possible Link to Microseismicity Along Ultraslow Spreading Ridges? J. Geophys. Res. Solid Earth 125, 1–24. https://doi.org/10.1029/2020JB019509

Whitney, D.L., Evans, B.W., 2010. Abbreviations for names of rock-forming minerals. Am. Mineral. 95, 185–187. https://doi.org/10.2138/am.2010.3371

Yu, Z., Li, J., Niu, X., Rawlinson, N., Ruan, A., Wang, W., Hu, H., Wei, X., Zhang, J., Liang, Y., 2018. Lithospheric Structure and Tectonic Processes Constrained by Microearthquake Activity at the Central Ultraslow-Spreading Southwest Indian Ridge (49.2° to 50.8°E). J. Geophys. Res. Solid Earth 123, 6247–6262. https://doi.org/10.1029/2017JB015367

TABLES

Table 1: Representative spot analyses of amphibole compositions for the four types of amphibole-bearing samples from the Eastern SWIR: neoblasts in Fig. 3b, 7d-e (marked points) in GSR zones; neoblasts in Fig. 4b and in shear zones in Fig. 7f (marked points) in melt-impregnated ultramafic samples; porphyroclasts and neoblasts in Fig. 5b-c for amphibole mylonites; and fibrous amphiboles in Fig. 5e and undeformed amphiboles in Fig. 5f for serpentinized ultramafic samples. The whole amphibole data set is in Table A4.

thin section	amphibole-bearing type	mineral	position	SiO2	TiO2	Al2O3	FeO	MnO	MgO	CaO	Na2O	K2O	Cr2O3	NiO	Cl	F	TOTAL	Mg#	Al T	(Na+K)A	Si
SMS_DR10_4_8A	amphibole-bearing GSR zone	amphibole 13	neoblast	53.38	0.20	4.03	2.26	0.11	21.76	13.99	0.78	0.00	0.58	0.06	0.05	0.00	97.20	94.48	0.57	0.21	7.43
SMS_DR10_4_8A	amphibole-bearing GSR zone	amphibole 14	neoblast	51.88	0.26	5.76	2.57	0.02	22.47	11.40	1.21	0.01	0.74	0.12	0.07	0.00	96.53	93.97	0.75	0.33	7.25
SMS_DR10_4_8A	amphibole-bearing GSR zone	amphibole 16	neoblast	52.48	0.18	3.90	2.69	0.05	23.73	11.41	0.81	0.01	0.50	0.07	0.06	0.00	95.89	94.03	0.62	0.22	7.38
SMS_DR10_4_8A	amphibole-bearing GSR zone	amphibole V2	vein	51.43	0.21	7.94	3.85	0.02	20.38	12.51	1.67	0.03	0.60	0.08	0.00	0.00	98.69	90.43	0.90	0.43	7.10
SMS_DR10_4_8A	amphibole-bearing GSR zone	amphibole V3	vein	49.76	0.14	9.65	3.51	0.06	19.56	12.45	2.13	0.01	0.72	0.00	0.00	0.00	98.00	90.84	1.07	0.51	6.93
SMS_DR10_4_8A	amphibole-bearing GSR zone	amphibole V3	vein	52.18	0.16	5.96	3.55	0.04	23.56	11.37	1.25	0.01	0.37	0.00	0.00	0.00	98.45	92.21	0.82	0.34	7.18
SMS_DR10_4_8A	amphibole-bearing GSR zone	amphibole V4	vein	53.20	0.11	5.90	2.33	0.04	21.60	12.60	1.27	0.02	0.48	0.00	0.00	0.00	97.54	94.29	0.65	0.30	7.35
SMS_DR17_4_06	amphibole-bearing GSR zone	amphibole4	neoblast	53.23	0.11	6.23	2.93	0.00	22.09	12.36	1.23	0.02	0.45	0.11	0.03	0.00	98.79	93.07	0.72	0.33	7.28
SMS_DR17_4_06	amphibole-bearing GSR zone	amphibole5	neoblast	53.46	0.06	5.62	2.80	0.00	22.38	12.52	1.11	0.01	0.34	0.14	0.03	0.00	98.48	93.44	0.67	0.30	7.33
SMS_DR17_4_06	amphibole-bearing GSR zone	amphibole7	neoblast	52.11	0.03	7.15	3.08	0.05	21.56	12.59	1.44	0.02	0.28	0.04	0.03	0.00	98.37	92.59	0.82	0.39	7.18
SMS_DR29_4_6	amphibole-bearing melt-impregnated ultramafic	amphibole 3	neoblast	46.00	0.26	11.70	3.76	0.06	18.99	11.99	3.01	0.08	1.48	0.02	0.13	0.03	97.52	90.00	1.50	0.76	6.50
SMS_DR29_4_6	amphibole-bearing melt-impregnated ultramafic	amphibole 4	neoblast	46.50	0.22	11.71	3.64	0.03	19.24	12.08	2.94	0.03	1.63	0.16	0.13	0.00	98.33	90.41	1.48	0.75	6.52
SMS_DR29_5_31	amphibole-bearing melt-impregnated ultramafic	amphibole 9	post	57.28	0.12	2.18	1.97	0.06	22.96	13.16	0.79	0.03	0.19	0.09	0.04	0.00	98.87	95.40	0.24	0.14	7.76
SMS_DR29_5_31	amphibole-bearing melt-impregnated ultramafic	amphibole 9	post	58.62	0.06	0.65	1.89	0.06	23.46	12.73	0.91	0.02	0.00	0.10	0.00	0.00	98.49	95.68	0.06	0.12	7.94
SMS_DR29_5_31	amphibole-bearing melt-impregnated ultramafic	amphibole 10	porphyroclast	52.13	0.30	6.27	2.39	0.00	20.97	12.94	2.16	0.07	0.99	0.16	0.02	0.00	98.41	93.99	0.79	0.51	7.21
SMS_DR29_5_31	amphibole-bearing melt-impregnated ultramafic	amphibole 11	porphyroclast	51.30	0.39	6.87	2.81	0.07	20.63	12.72	2.36	0.01	0.99	0.03	0.04	0.00	98.23	92.90	0.88	0.53	7.12
SMS_DR27_3_20	amphibole mylonite	amphibole 7	porphyroclast	50.06	2.07	7.63	3.83	0.05	20.38	11.92	2.34	0.02	0.32	0.17	0.07	0.08	98.94	90.46	1.08	0.47	6.92
SMS_DR27_3_20	amphibole mylonite	amphibole 8	neoblast	49.82	1.21	7.74	3.28	0.05	20.48	12.17	2.20	0.02	1.38	0.13	0.08	0.07	98.61	91.76	1.09	0.48	6.91
SMS_DR27_3_20	amphibole mylonite	amphibole 9	neoblast	49.10	2.01	8.37	3.58	0.07	19.91	12.27	2.34	0.03	1.13	0.13	0.09	0.00	99.03	90.85	1.19	0.52	6.81
SMS_DR33_2_7	amphibole mylonite	amphibole 1	porphyroclast	46.77	3.06	7.78	11.56	0.26	16.16	9.63	2.83	0.27	0.05	0.10	0.02	0.16	98.65	71.36	1.28	0.59	6.72
SMS_DR33_2_7	amphibole mylonite	amphibole 1	porphyroclast	46.59	3.12	7.83	11.32	0.22	15.96	9.87	2.83	0.28	0.00	0.05	0.01	0.00	98.06	71.53	1.25	0.66	6.75
SMS_DR33_2_7	amphibole mylonite	amphibole 2	neoblast	49.45	1.04	8.31	3.89	0.04	20.21	11.67	2.58	0.12	0.32	0.15	0.05	0.05	97.88	90.26	1.09	0.58	6.91
SMS_DR29_4_7	amphibole-bearing serpentinized peridotite	amphibole3	post	52.71	0.12	5.18	2.47	0.05	22.15	12.12	1.80	0.05	0.95	0.13	0.05	0.00	97.78	94.12	0.70	0.44	7.30
SMS_DR29_4_7	amphibole-bearing serpentinized peridotite	amphibole3	post	55.45	0.11	3.26	2.17	0.00	22.71	12.94	1.14	0.03	0.56	0.09	0.02	0.06	98.55	94.91	0.43	0.24	7.57
SMS_DR29_4_7	amphibole-bearing serpentinized peridotite	amphibole4	porphyroclast	56.24	0.01	2.76	2.15	0.04	23.07	13.27	0.96	0.03	0.06	0.13	0.01	0.05	98.78	95.02	0.35	0.23	7.65
SMS_DR29_4_7	amphibole-bearing serpentinized peridotite	amphibole5	deformed acicular	55.82	0.13	3.09	2.60	0.05	23.14	12.64	1.13	0.03	0.06	0.00	0.01	0.08	98.76	94.08	0.41	0.24	7.59
SMS_DR29_4_7	amphibole-bearing serpentinized peridotite	amphibole7	deformed acicular	56.88	0.09	2.11	2.25	0.07	23.40	12.60	0.83	0.02	0.05	0.05	0.00	0.10	98.44	94.87	0.28	0.14	7.72
SMS_DR29_4_7	amphibole-bearing serpentinized peridotite	amphibole8	deformed acicular	57.44	0.13	1.99	2.02	0.02	23.10	13.01	0.65	0.02	0.02	0.12	0.00	0.09	98.60	95.32	0.22	0.08	7.78

806 **FIGURES**

807 **FIGURE 1**

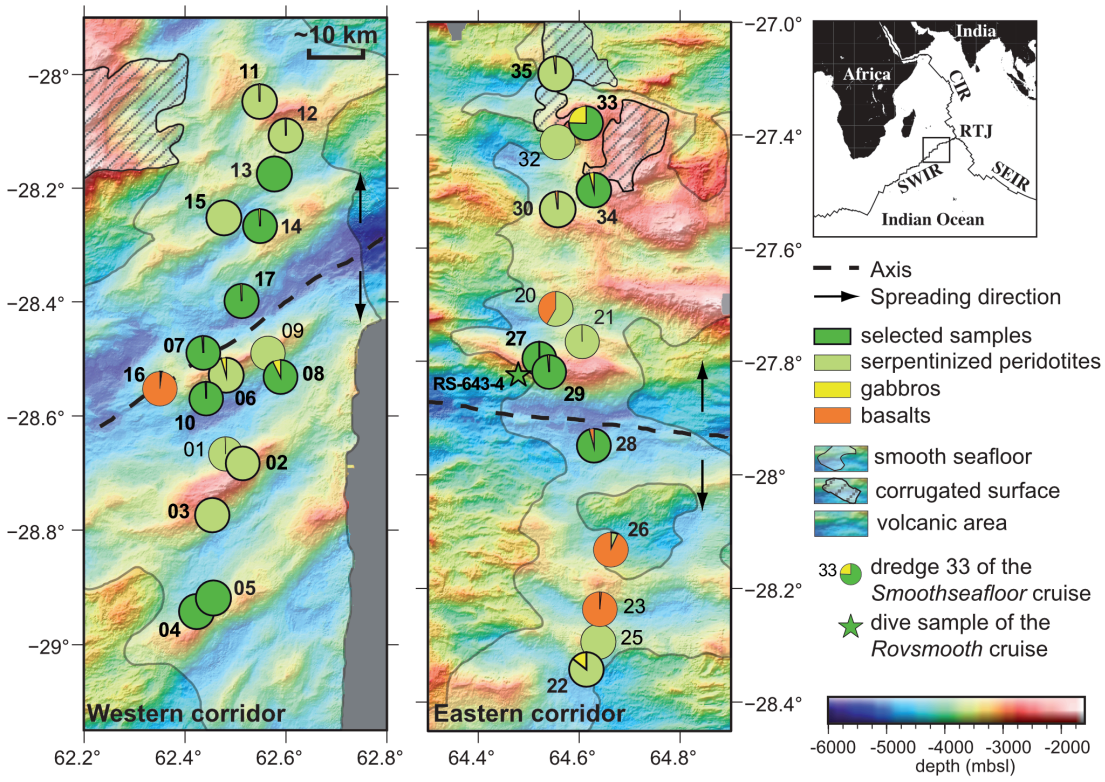

808

809

810 FIGURE 1: (a) Bathymetric maps of the two nearly-amagmatic spreading corridors of the
811 eastern Southwest Indian Ridge (62-65°E). Smooth and corrugated surfaces are highlighted in
812 white and dashed areas, respectively. Samples were dredged on- and off-axis (black dashed
813 line) during the *Smoothseafloor* cruise (doi: 10.17600/10200050, Table A1). Map is modified
814 from Rouméjon et al., 2015 (after Sauter et al., 2013). Pie charts show proportions of dredged
815 samples recovered by rock type. Dredges that recovered amphibole-bearing peridotites are
816 shown in thicker contours, and those in which amphibole-bearing samples were analyzed for
817 this study are shown in dark green. The green star indicates the position of sample RS-643-4,
818 which was sampled *in-situ* during a ROV dive on the wall of the active detachment (*Rovsmooth*
819 cruise, doi: 10.17600/16002000; Table A1).

820

821 **FIGURE 2**

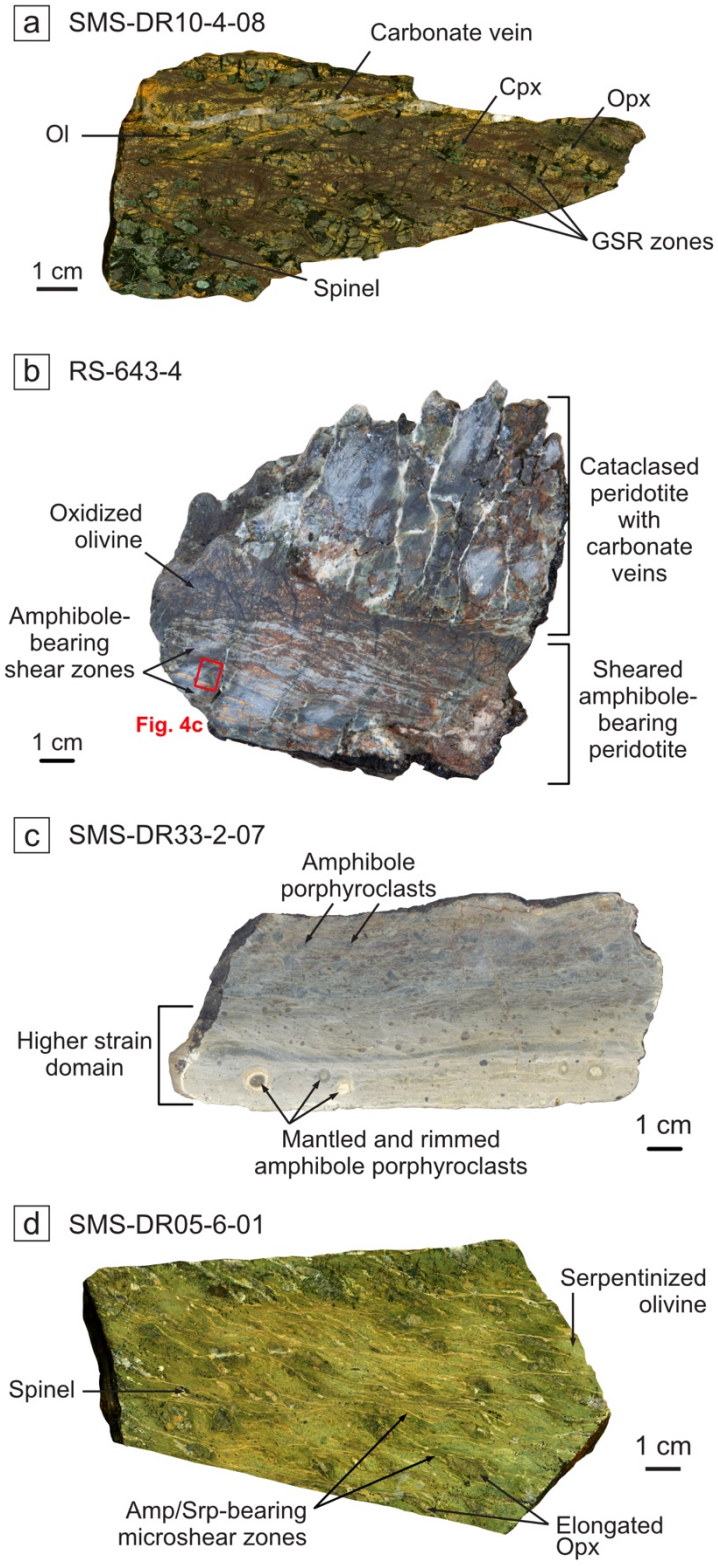

822

823 Figure 2: Photographs of selected amphibole-bearing ultramafic rocks from the Eastern SWIR.

824 (a) Deformed partially serpentinized lherzolite (sample SMS-DR10-4-08). Texture is strongly

825 foliated with elongated porphyroclasts of orthopyroxene (Opx) and clinopyroxene (Cpx), and
826 anastomosed grain size reduction (GSR) zones that locally contain amphibole (see Fig. 3;
827 Bickert et al., 2021). Olivine (Ol) is partially replaced by oxidized minerals. Primary mineralogy
828 is cut by late veins of carbonates. (b) Cataclased melt-impregnated peridotite, partially
829 replaced by oxidized minerals, with amphibole-bearing shear bands clustered along
830 orthopyroxene grains (sample RS-643-4). The red square outlines the location of Figure 4c. (c)
831 Amphibole mylonite (sample SMS-DR33-2-07). Brown amphibole porphyroclasts in the most
832 deformed part of the sample form rolling structures (δ-/σ-types) enclosed in a very fine-
833 grained matrix of amphibole, chlorite and talc. (d) Foliated amphibole-bearing serpentinized
834 peridotite (sample SMS-DR05-6-01). Shear zones of amphibole (Amp) and serpentine (Srp)
835 underline the foliation. Olivine is fully replaced by serpentine (Srp).
836
837

838 **FIGURE 3**

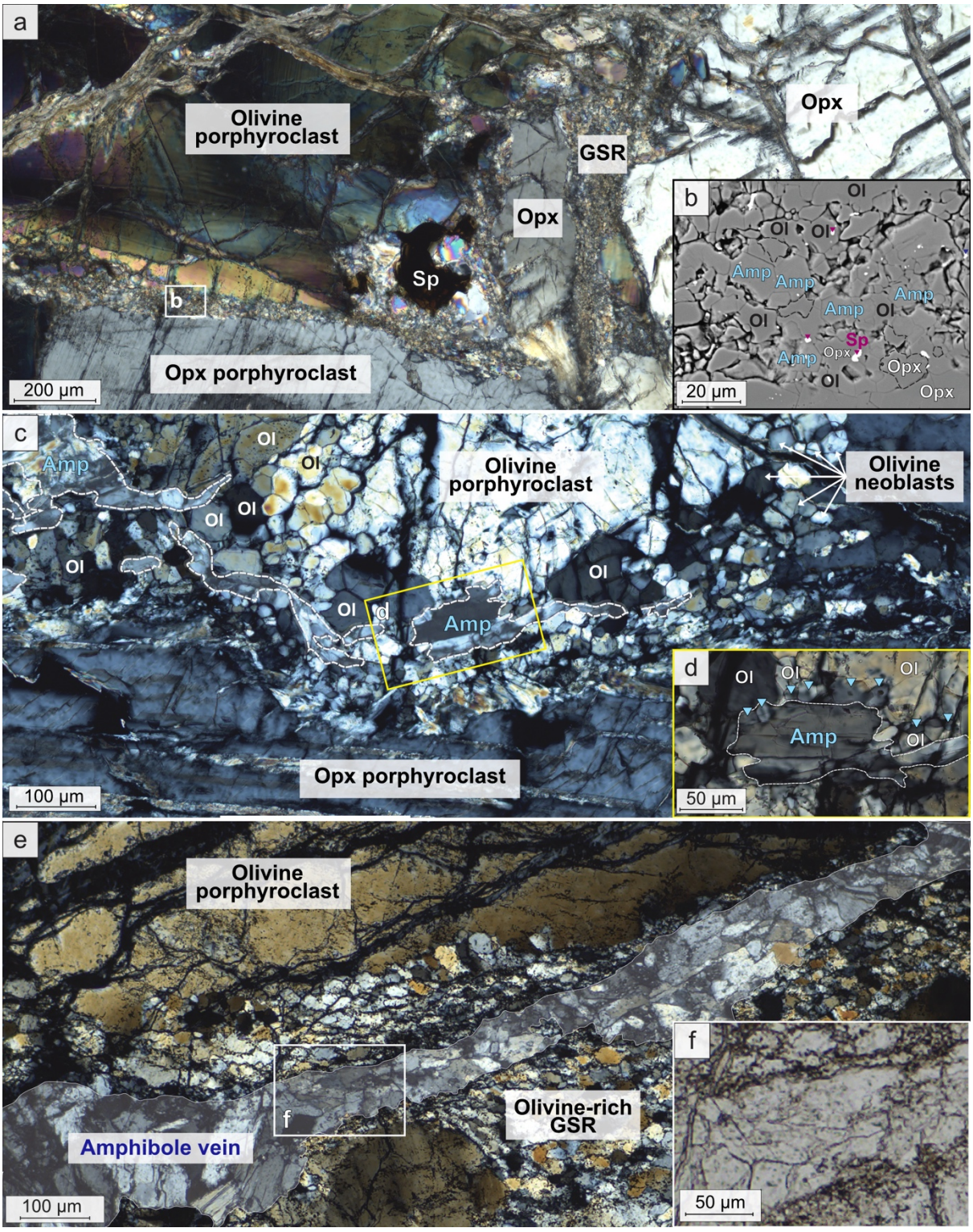

839

840 Figure 3: Amphiboles in Grain Size Reduction (GSR) zones. Microphotographs under cross-
841 polarized light (a, c-e) and SEM images (b). (a) Microphotography of a GSR zone at contact
842 between olivine and orthopyroxene porphyroclasts (sample SMS-DR17-4-6). (b) SEM detail of

843 the recrystallized assemblage composed of olivine (Ol) + spinel (Sp) + orthopyroxene (Opx) +
844 polygonal amphiboles (Amp) (modified from Bickert et al., 2021). (c) Coarser prismatic
845 amphiboles in an olivine-rich GSR zone (sample SMS- DR08-2-26). (d) Detail of the same GSR
846 zone showing small polygonal amphibole and olivine crystals crystallizing together at contact
847 with a coarser prismatic amphibole. (e, f) Undeformed vein of tabular and prismatic
848 amphiboles crosscutting an olivine-rich GSR domain (sample SMS-DR10-4-08).
849

FIGURE 4

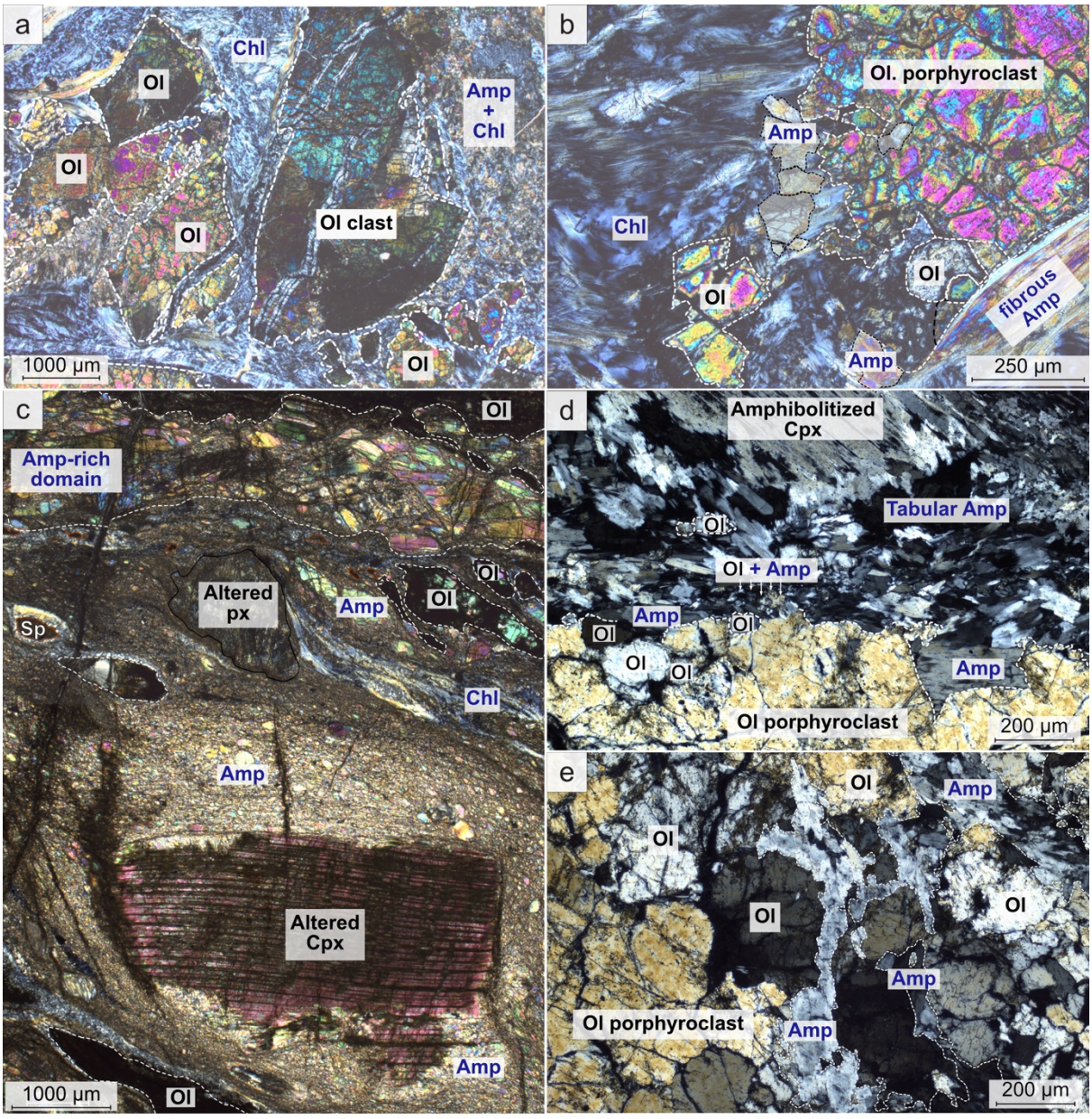

FIGURE 4: Amphibole-bearing melt-impregnated peridotites. Microphotographs under cross-polarized light. (a) Microshear zones enclosing clasts of olivine (Ol) fragments in a matrix of fibrous to primastic amphibole (Amp) and chlorite (Chl) (sample SMS-DR29-4-06). (b) Detail of the contact between olivine (Ol) and the matrix. Locally, olivine recrystallizes in coarse grains with prismatic amphibole (Amp). Fibrous amphibole crosscut olivine neoblasts, postdating the deformation (lower right side of the picture). (c) Example of a sample (sample RS-643-04) with thicker amphibole-rich domains composed of elongated and deformed amphibole

859 porphyroclasts. Amphibole-bearing shear zones are mostly focused along pyroxene
860 porphyroclasts. (Clino-)pyroxene (Cpx) porphyroclasts are partially to fully replaced by syn-
861 deformation amphibole. Relicts of olivine (Ol) and spinel (Sp) have elongated shapes and are
862 enclosed in a matrix of prismatic to fibrous amphibole (Amp) and chlorite (Chl). The elongated
863 size of pyroxenes and spinel porphyroclasts suggest a HT primary shear zone that has been
864 subsequently altered. (d) Late amphibole shear zones at contact with olivine and
865 clinopyroxene porphyroclasts (sample SMS-DR29-7-01). Clinopyroxene (Cpx) is fully replaced
866 by tabular amphiboles (Amp) similar to the ones surrounding it. Olivine (Ol) remains fresh with
867 slightly corroded / blurred boundaries at contact with amphibole shear zones, due to local
868 recrystallization of olivine and amphibole. (e) Interstitial, prismatic undeformed amphiboles
869 along olivine grain boundaries in the same sample (SMS-DR29-7-01).
870

FIGURE 5

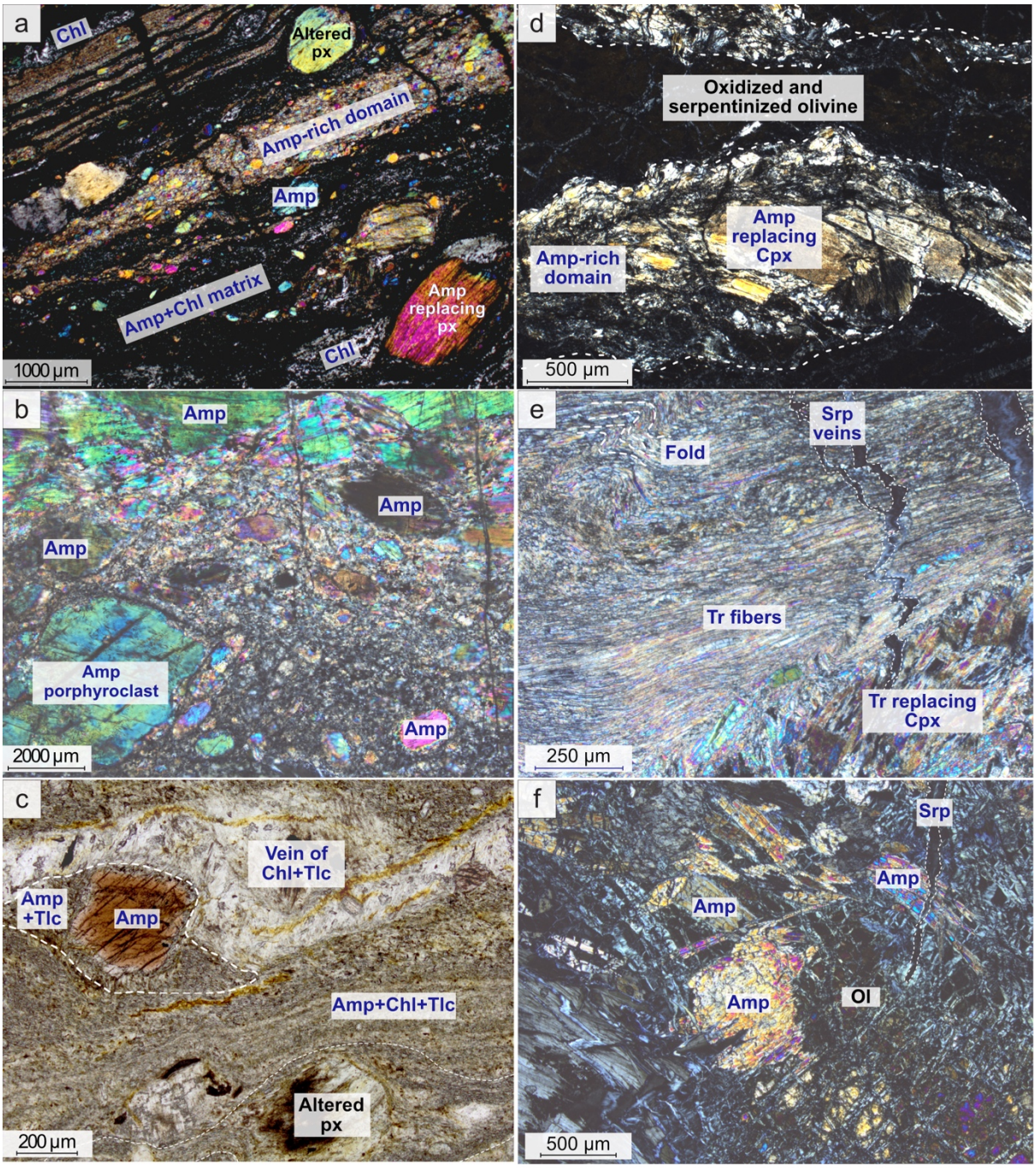

FIGURE 5: Amphibole mylonites (a-c) and amphibole-bearing serpentinized peridotites (d-f). Microphotographs under cross-polarized (a-b, d-f) and natural light (c). (a) Alternation of amphibole-rich domains with polymineralic domains. Pyroxenes (px) are entirely replaced by amphibole (amp; sample SMS-DR13-4-41). (b) Amphibole-rich domains are composed of deformed porphyroclasts of amphibole in a matrix of amphibole neoblasts (sample SMS-

878 DR27-3-20). (c) Polymineralic domains are composed of porphyroclasts of brown amphiboles
879 and altered pyroxenes forming complex rolling structures (δ- to σ-types) in a matrix of
880 amphibole (Amp) ± chlorite (Chl) ± talc (Tlc). Locally, veins of chlorite (Chl) and talc (Tlc) follow
881 the foliation (sample SMS-DR33-2-07). (d) In amphibole-bearing serpentinized peridotites,
882 primary minerals such as olivine (Ol) and pyroxenes (px) are almost completely altered or
883 replaced by amphibole (Amp; sample SMS-DR13-4-41). Amphibole and the replaced pyroxene
884 porphyroclasts can locally be fragmented in a domino type /shear band type. (e) Detail of a
885 late shear zone of fibrous tremolite (Tr), in contact with weakly deformed peridotite in which
886 clinopyroxene (Cpx) is replaced by tabular to prismatic amphiboles (Amp; sample SMS-DR29-
887 4-07). Serpentine (Srp) veins cut the amphibole shear zones, postdating amphibole
888 deformation. (f) Detail of undeformed tabular to prismatic amphibole in olivine groundmass
889 cut by serpentine (Srp) fractures (sample SMS-DR29-4-07).
890

FIGURE 6

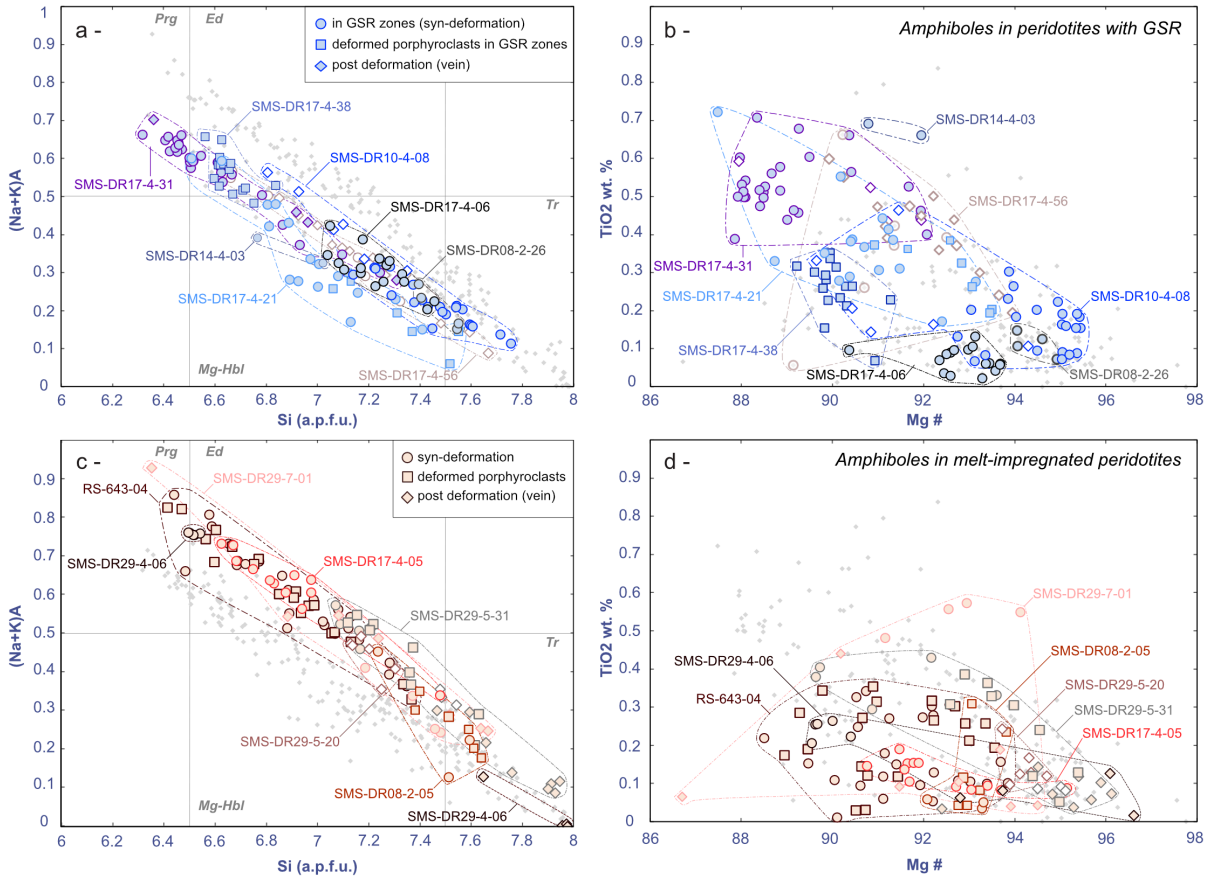

FIGURE 6: Amphibole compositions in (a, b) peridotites with amphibole-bearing GSR zones and (c, d) amphibole-bearing melt-impregnated peridotites. (a, c) Alkali versus Si content in atom per formula unit (a.p.f.u.). (b, d) TiO_2 (wt.%) versus Mg#. The grey data points represent the whole amphibole dataset presented in this study (Table A4). Abbreviations taken from Whitney and Evans (2010): pargasite (Prg), edenite (Ed), magnesiohornblende (Mg-Hbl), tremolite (Tr).

FIGURE 7

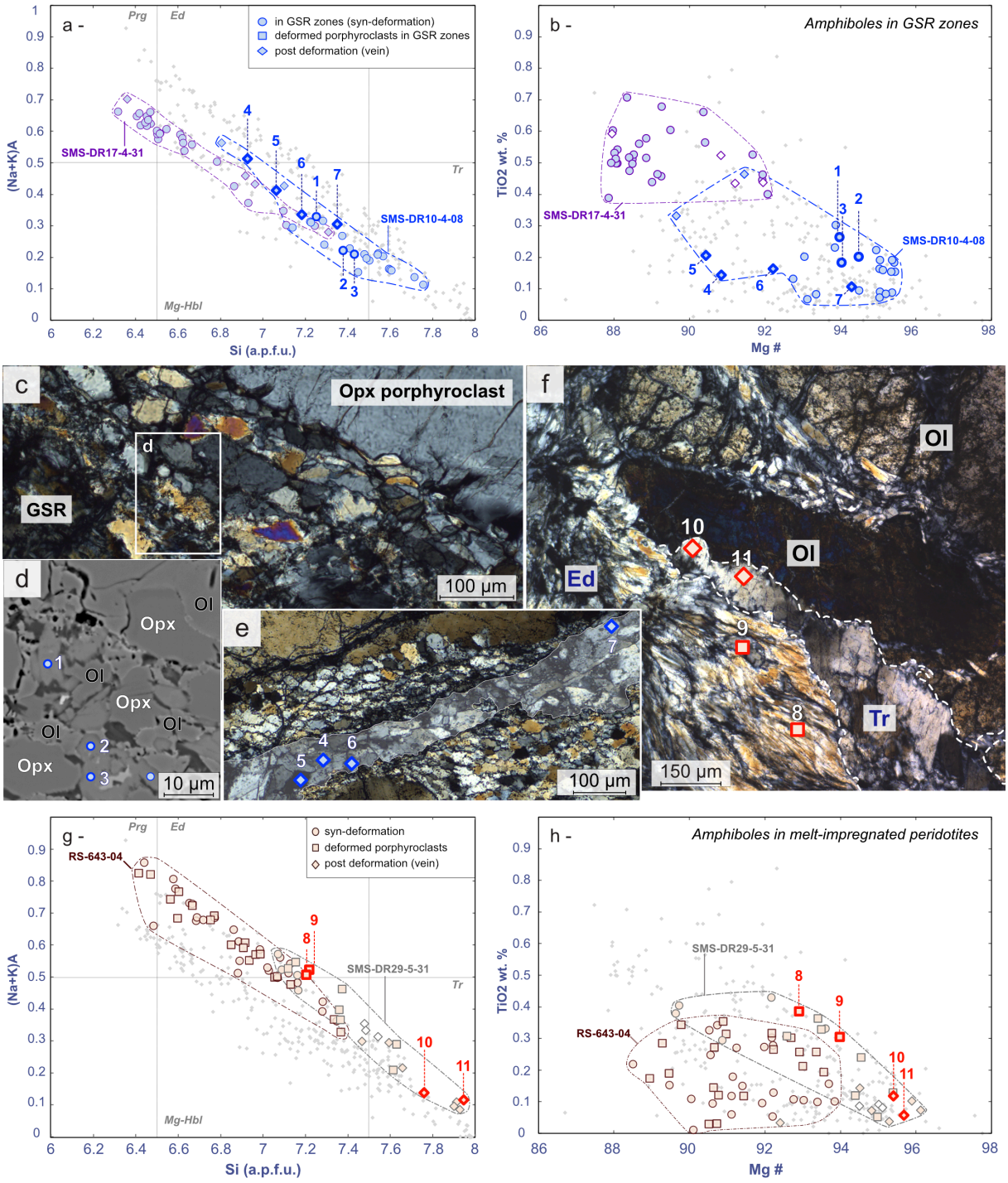

Figure 7: Intrasample variations in amphibole composition in (a-b) two samples with amphibole-bearing GSR zones (samples SMS-DR10-4-08 and SMS-DR17-4-31) and (g-h) two amphibole-bearing melt-impregnated peridotites (samples SMS-DR29-5-31 and RS-643-04, the latter shown in Fig. 2b, 4c). Corresponding microphotographs and SEM images in (c-f):

numbers correspond to measurements highlighted in the graphs (a-b, g-h) and reported in Table 1. (a, g) Alkali versus Si content in atom per formula unit (a.p.f.u.). (b, h) TiO_2 (wt.%) versus Mg#. The grey data points represent the whole amphibole dataset presented in this study (Table A4). (c) Microphotograph under polarized light of a polymineralic amphibole-bearing GSR zone along an orthopyroxene (Opx) porphyroclast (sample SMS-DR10-4-08). (d) Detail of the recrystallized assemblage composed of olivine (Ol), Orthopyroxene (Opx) and polygonal amphibole (blue points). (e) Amphibole vein crosscutting an olivine-rich GSR zone (see Figure 3e; same sample). (f) Amphibole microshear zone in an amphibole-bearing impregnated ultramafic sample, showing deformed crystals, rimmed by undeformed amphibole at contact with olivine (sample SMS-DR29-5-31).

FIGURE 8

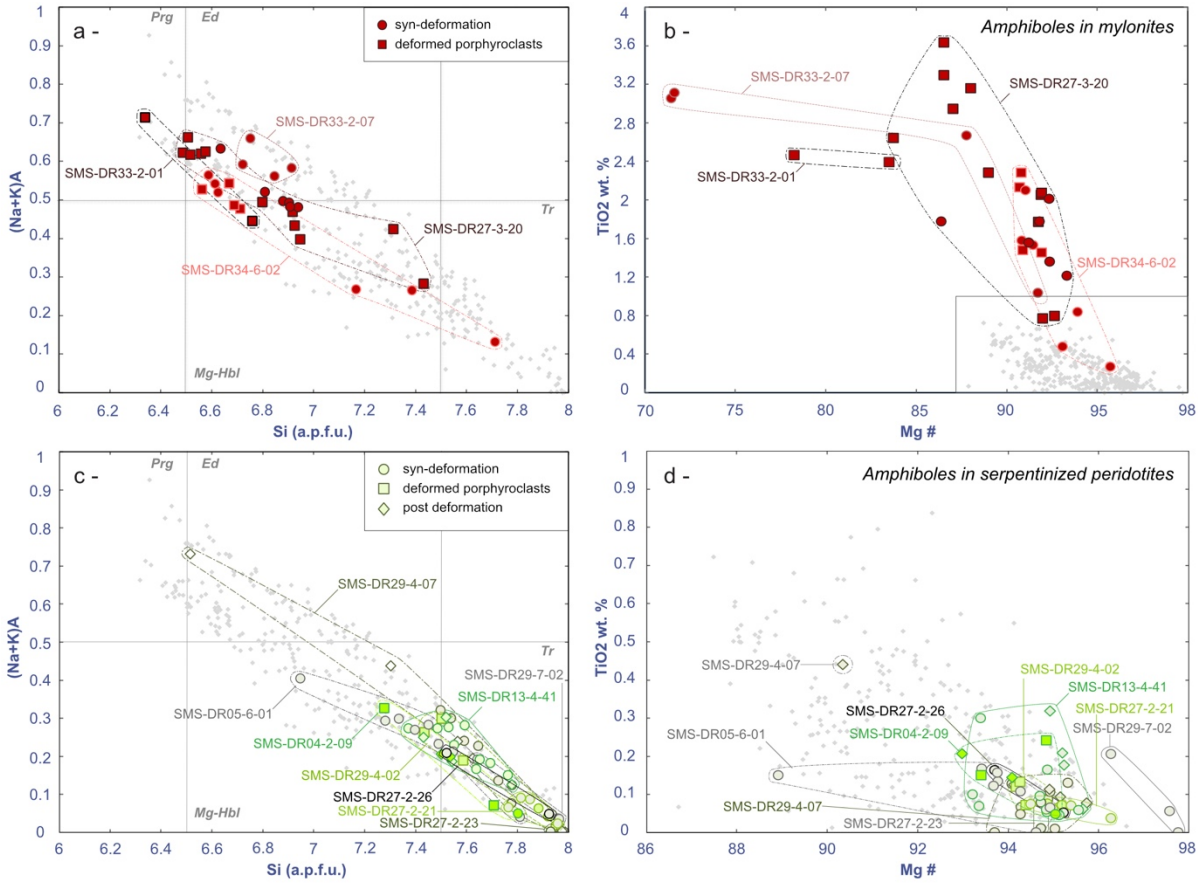

Figure 8: Amphibole compositions in (a, b) amphibole mylonites and (c, d) amphibole-bearing serpentinized peridotites. (a, c) Alkali versus Si content in atom per formula unit (a.p.f.u.). (b, d) TiO_2 (wt.%) versus Mg#. The grey data points represent the whole amphibole data set presented in this study (Table A4). Abbreviations taken from Whitney & Evans (2010): pargasite (Prg), edenite (Ed), magnesiohornblende (Mg-Hbl), tremolite (Tr).

FIGURE 9

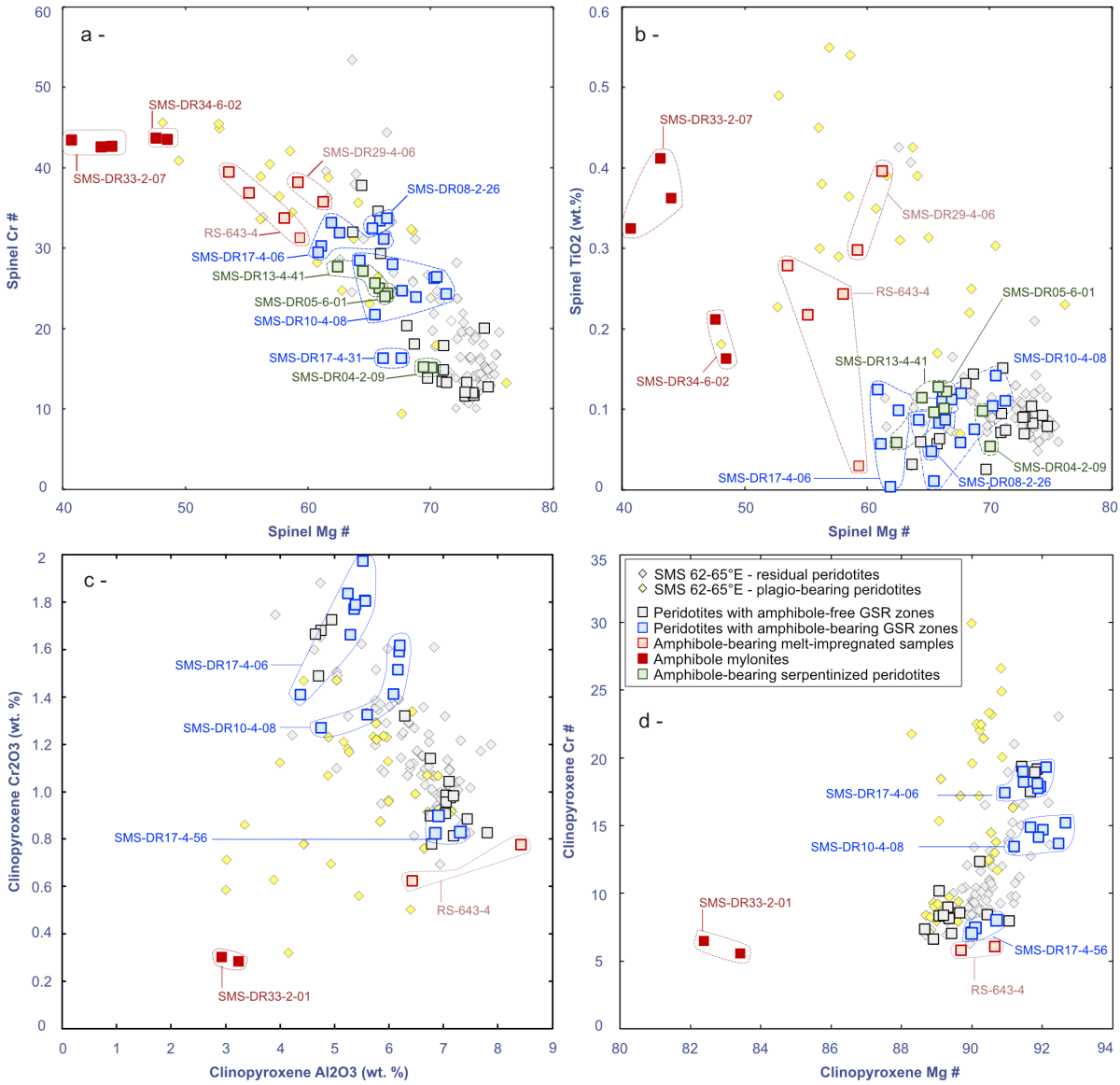

FIGURE 9: Spinel and clinopyroxene core compositions in amphibole-bearing samples (data in Tables A5-A6, respectively). (a) Spinel Cr# versus Mg# values. (b) Spinel TiO_2 (wt.%) versus Mg#. (c) Clinopyroxene Cr_2O_3 content (wt.%) vs Al_2O_3 (wt.%). (d) Clinopyroxene Mg# versus Cr# values. Residual and plagioclase-bearing peridotites from the Eastern SWIR (data from Seyler et al., 2003; Paquet et al., 2016 and unpublished data from D.Brunelli) are shown for comparison.

FIGURE 10

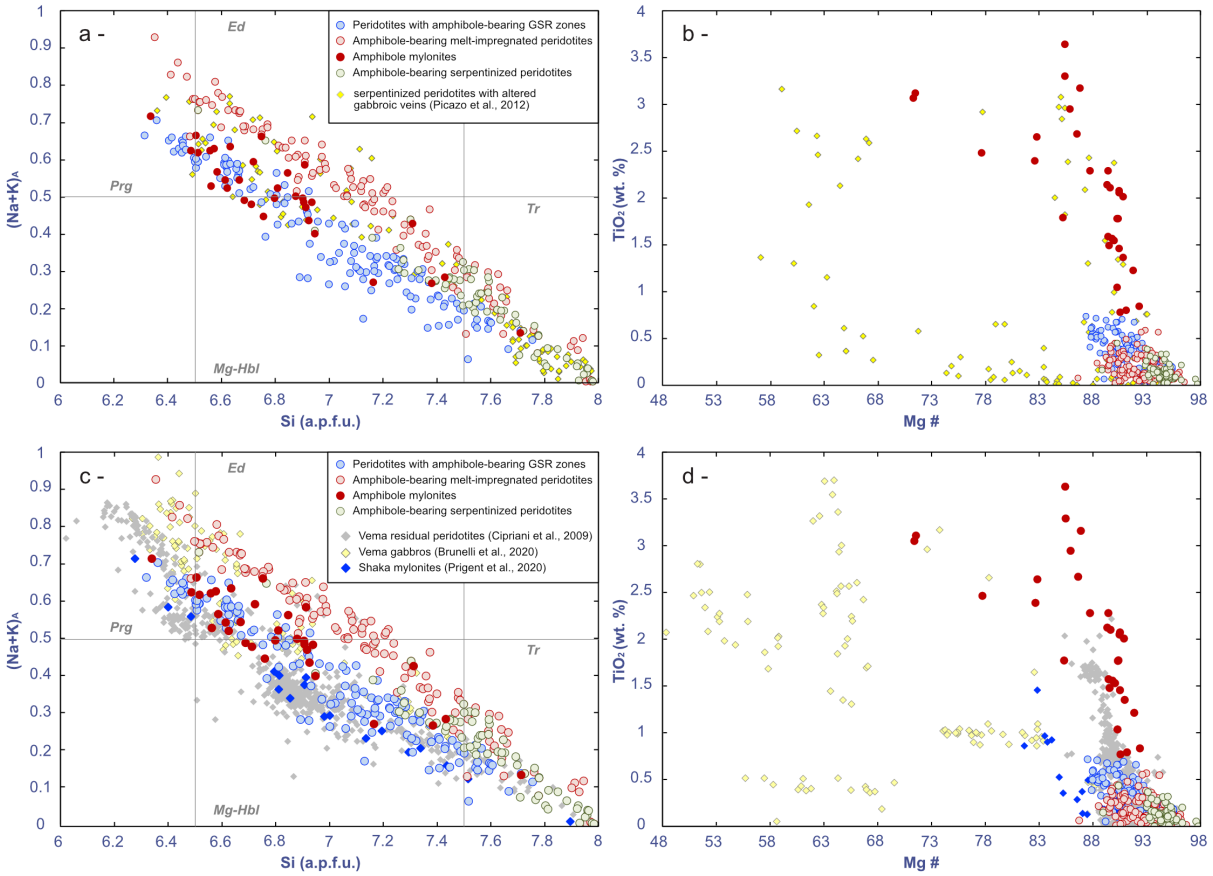

FIGURE 10: Compositional variability of amphiboles in SWIR amphibole-bearing samples (Table A4) compared to (a,b) amphibole-bearing serpentinized peridotites with altered gabbroic veins from the MAR at 15°N (Picazo et al., 2012) and (c, d) amphibole-bearing peridotites and gabbros from the Shaka (Prigent et al., 2020) and Vema Transform Zones (Cipriani et al., 2009; Brunelli et al., 2020). Color code is the same as in Figures 6-9. (a) alkali versus Si content in atom per formula unit (a.p.f.u.) and (b) TiO_2 (wt.%) versus Mg#. Abbreviations taken from Whitney & Evans (2010): pargasite (Prg), edenite (Ed), magnesiohornblende (Mg-Hbl), tremolite (Tr).

FIGURE 11

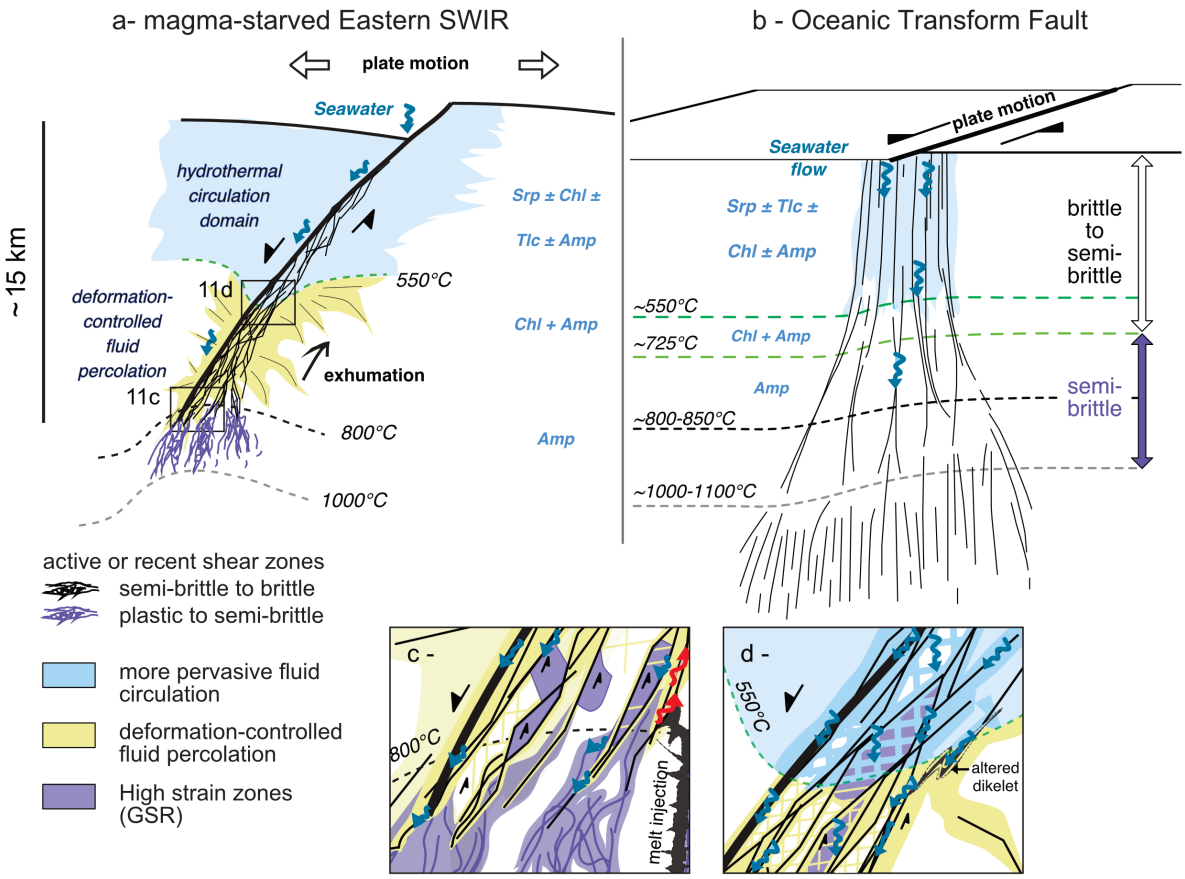

FIGURE 11: Interpretative sketches comparing hydration and deformation processes in the root zone of (a) the eastern SWIR detachment faults (modified after Bickert et al., 2021) and (b) oceanic transform faults (modified after Prigent et al., 2020). (c-d) are details of (a) showing fluid circulation (c) at the root zone of detachment faults and (d) at the transition to greenschist conditions. In (c), fractures and microfractures forming the detachment (black lines) root into a system of anastomosing plastic to semi brittle shear zones (dark purple), forming high strain zones (light purple). Locally, microfractures forming the detachment enclose blocks of deformed material, which will be progressively exhumed with fault activity. Seawater-derived fluids percolate through the network of microfractures forming the detachment and through mineral scale heterogeneities (blue arrows), while magma-derived

fluids move up along the deformation system (red arrows). In (d), as mantle blocks are exhumed along the network of faults forming the detachment, under greenschist conditions, hydration becomes more pervasive. Magmatic minerals from gabbroic dikelets form minerals weaker than serpentine, favoring strain localization and fluid focusing.

SUPPLEMENTARY TABLES

Table A1: Depths and positions of the dredges containing amphibole-bearing ultramafic rocks and of the one amphibole-bearing sample collected in-situ (sample RS-643-04). Dredges were done on- and off-axis during *Smoothseafloor* cruise (2010; doi: 10.17600/10200050). Positions are based on on-bottom/off-bottom positions and recalculated from ship positions. Sample RS-643-04 was recovered in-situ during *Rovsmooth* cruise (2016; doi:10.17600/16002000). Abbreviations: longitude (long.), and latitude (lat.).

Sampling method	Name	Long. E, Start	Lat. N, Start	Depth (m), Start	Long. E, End	Lat. N, End	Depth (m), End	Weight (kg)	Total number of samples	Number of peridotite samples
Dredge	DR02	62°30.26'E	28°40.89'S	-2979	62°30.98'E	28°41.29'S	-2476	512	19	19
Dredge	DR03	62°27.41'E	28°46.79'S	-3727	62°26.51'E	28°46.39'S	-3177	80	24	24
Dredge	DR04	62°25.63'E	28°56.57'S	-3673	62°24.58'E	28°57.19'S	-3224	14.60	12	12
Dredge	DR05	62°27.52'E	28°55.57'S	-2677	62°25.35'E	29°01.49'S	-3320	655	104	104
Dredge	DR06	62°29.13'E	28°31.87'S	-3630	62°29.00'E	28°31.52'S	-3238	166	57	22
Dredge	DR07	62°26.30'E	28°29.75'S	-4186	62°26.45'E	28°30.03'S	-3817	390	46	42
Dredge	DR08	62°35.13'E	28°31.29'S	-4672	62°35.25'E	28°30.55'S	-4370	722	48	30
Dredge	DR10	62°27.74'E	28°33.22 S	-4319	62°28.11'E	28°33.55'S	-3602	27	31	28
Dredge	DR11	62°33.09'E	28°03.09'S	-3906	62°33.30'E	28°03.40'S	-3145	60.1	39	38
Dredge	DR12	62°36.18'E	28°06.48'S	-3909	62°36.22'E	28°06.10'S	-3468	44	36	35
Dredge	DR13	62°34.74'E	28°11.17'S	-3927	62°34.24'E	28°10.16'S	-3608	122	43	42
Dredge	DR14	62°33.02'E	28°16.15'S	-3968	62°33.17'E	28°16.42'S	-3375	105	30	28
Dredge	DR15	62°28.55'E	28°15.17'S	-4298	62°28.46'E	28°15.34'S	-4059	234.2	33	28
Dredge	DR16	62°21.11'E	28°33°32'S	-4360	62°21.43'E	28°32.63'S	-3838	286	25	11
Dredge	DR17	62°30.55'E	28°24.32'S	-4963	62°31.19'E	28°23.86'S	-4392	235	101	82
Dredge	DR22	64°36.59'E	28°20.28'S	-4443	64°36.39'E	28°19.27'S	-3916	28	30	21
Dredge	DR23	64°38.00'E	28°14.40'S	-4252	64°38.00'E	28°13.55'S	-3785	61.5	14	0
Dredge	DR24	64°32.51'E	28°11.87'S	-4028	64°32.66'E	28°11.18'S	-3390	80	8	0
Dredge	DR25	64°37.80'E	28°18.08'S	-3762	64°37.10'E	28°17.41'S	-	0.7	1	1
Dredge	DR26	64°39.32'E	28°07.95'S	-4101	64°38.79'E	28°08.98'S	-3712	386	32	12
Dredge	DR27	64°31.19'E	27°.47.98'S	-3203	64°31.83'E	27°48.61'S	-2570	810	61	60
Dredge	DR28	64°37.22'E	27°56.80'S	-4760	64°38.02'E	27°57.41'S	-4542	90	19	14
Dredge	DR29	64°32.01'E	27°49.31'S	-2956	64°33.29'E	27°49.08'S	-2604	930	95	79
Dredge	DR30	64°33.41'E	27°32.54'S	-2950	64°33.39'E	27°33.12'S	-2734	90	14	13
Dredge	DR33	64°36.03'E	27°22.83'S	-2856	64°35.53'E	27°22.49'S	-2504	170	43	34
Dredge	DR34	64°36.98'E	27°30.29'S	-2928	64°37.73'E	27°29.54'S	-2583	400	77	69
Dredge	DR35	64°32.60'E	27°17.82'S	-4350	64°32.61'E	27°17.24'S	-3862	41.3	25	20
In-situ	RS-643-04	64°31.70'E	27°48.44'S	-2690	-	-	-		1	1

Table A2: Proportions of amphibole-bearing samples in a set of 386 ultramafic samples collected at the Eastern SWIR (62-65°E) during *Smoothseafloor* and *Rovsmooth* cruises (see text and caption of Table A1).

Dredge	Number of ultramafic samples	Samples with GSR zones	Amphibole in GSR zones	Chlorite-bearing samples	Chlorite-bearing samples with amphibole	Amphibole mylonites	Amphibole-bearing serpentinized peridotites
SMS-DR1	6	-	-	-	-	-	-
SMS-DR2	6	3	-	-	-	-	1
SMS-DR3	5	-	-	1	1	-	2
SMS-DR4	4	4	-	3	3	-	1
SMS-DR5	14	4	-	3	2	-	2
SMS-DR6	11	3	-	1	1	-	-
SMS-DR7	11	1	-	6	3	-	-
SMS-DR8	10	5	1	2	1	-	1
SMS-DR9	1	-	-	-	-	-	-
SMS-DR10	16	16	1	3	-	-	6
SMS-DR11	13	2	-	4	2	-	1
SMS-DR12	17	1	-	2	3	-	1
SMS-DR13	15	5	-	5	5	-	6
SMS-DR14	7	3	1	1	1	-	3
SMS-DR15	14	1	-	1	1	-	-
SMS-DR16	4	-	-	1	1	-	1
SMS-DR17	44	12	6	11	11	-	1
SMS-DR20	3	-	-	-	-	-	-
SMS-DR21	7	-	-	-	-	-	-
SMS-DR22	17	3	-	1	-	-	3
SMS-DR26	4	-	-	1	1	-	-
SMS-DR27	34	8	-	13	5	1	3
SMS-DR28	10	1	-	4	4	-	-
SMS-DR29	48	26	-	29	22	-	4
SMS-DR30	9	2	-	4	3	-	-
SMS-DR32	3	-	-	-	-	-	-
SMS-DR33	15	7	-	4	3	2	-
SMS-DR34	28	4	-	4	3	5	3
SMS-DR35	9	8	-	1	1	-	-
RS-643-4	1	1	-	1	1	-	-
TOTAL	386	120	9	106	78	8	39
Proportion	-	31%	2%	27%	20%	2%	10%

Table A3: Name, terminations of IGSN code (http://www.igsn.org), amphibole-bearing and textural types and characteristics of samples selected in this study. Samples with GSR zones differ from amphibole mylonites by the proportion of GSR: GSR zones are very localized and well below the 50-90% proportions of matrix that define a mylonite.

			Primary mineralogy				Deformation			Interaction with primary minerals		amp-rich domain			chl-bearing shear zones		Amp post-deformation	
sample	IGSN code*	Amphibole-bearing type	Olivine relicts	fresh px (>10%)	plagio	Magmatic amp	Texture	Deformation types (A0-A3)	GSR	Polygonal amp in GSR	Recryst. amp + ol	oriented tabular amp	deformed prismatic amp porphyroclasts	oriented fibrous amp	amp + chl	fibrous chl ± srp	unoriented amp	mineralization after px
SMS_DR08_02_26	3484	amphibole-bearing GSR zones	yes	yes			Porphyroclastic	A2	x	x								
SMS_DR10_04_08	3530	amphibole-bearing GSR zones	yes	yes			Porphyroclastic	A3	x	x						x	vein	
SMS_DR14_04_03	3683	amphibole-bearing GSR zones	yes	yes			Porphyroclastic	A2	x	x						x		amp+px
SMS_DR17_04_06	3792	amphibole-bearing GSR zones	yes	yes			Porphyroclastic	A2	x	x								amp
SMS_DR17_04_21	3807	amphibole-bearing GSR zones	yes	yes			Porphyroclastic	A3	x	x	x	x	x			x		amp
SMS_DR17_04_31	3817	amphibole-bearing GSR zones	yes	yes			Porphyroclastic	A3	x	x								
SMS_DR17_04_38	3824	amphibole-bearing GSR zones	-	yes			Protomylonite	A4	x	x			x			x		amp-chl
SMS_DR17_04_56	3842	amphibole-bearing GSR zones	yes	yes			Porphyroclastic	A2	x	prismatic ?		x					x	amp
RS_643_4	1104	impregnated amphibole-bearing peridotite	yes	no			Protomylonite	A3	x			x	x		x	?		amp-chl
SMS_DR08_02_05	3463	impregnated amphibole-bearing peridotite	yes	no			Porphyroclastic	A2-A3	x		?		x		x			amp-chl
SMS_DR17_04_05	3791	impregnated amphibole-bearing peridotite	yes	no			Porphyroclastic	A2	x		x	x						amp-(chl?)
SMS_DR29_04_06	4148	impregnated amphibole-bearing peridotite	yes	yes			Porphyroclastic	A1	-		x			x	x	x		chl ?
SMS_DR29_05_20	4176	impregnated amphibole-bearing peridotite	yes	yes			Porphyroclastic	A2	x		?	x			x	x		amp-chl
SMS_DR29_05_31	4187	impregnated amphibole-bearing peridotite	yes	no			Porphyroclastic	A1	-		x	x	x		x			amp-chl
SMS_DR29_07_01	4215	impregnated amphibole-bearing peridotite	yes	-	?		Porphyroclastic	A1	-		x	x			x			amp-chl
SMS_DR27_03_20	4084	amphibole mylonite	-	-		yes	Mylonite	A4	amp			x	x		x			amp
SMS_DR33_02_01	4271	amphibole mylonite	-	-	prehnite	yes	Mylonite	A4	amp	x								
SMS_DR33_02_07	4277	amphibole mylonite	-	no	?	yes	Mylonite	A4	amp				x		amp-tlc			
SMS_DR34_06_02	4383	amphibole mylonite	-	-		yes	Mylonite	A4	amp			x	x		x			
SMS_DR04_02_09	3235	serpentinized amphibole-bearing peridotite	no	yes			Porphyroclastic	A2-A3	x				x			x		amp
SMS_DR05_06_01	3321	serpentinized amphibole-bearing peridotite	no	yes			Porphyroclastic	A2-A3	x			x				x		amp
SMS_DR13_04_41	3675	serpentinized amphibole-bearing peridotite	no	no			Porphyroclastic	A3	x				x		?	x		amp
SMS_DR27_02_21	4058	serpentinized amphibole-bearing peridotite	no	no			Porphyroclastic	A0-A1				x	x	x		x		amp-chl
SMS_DR27_02_23	4060	serpentinized amphibole-bearing peridotite	no	no			Porphyroclastic	A0-A1				x				x		amp
SMS_DR27_02_26	4063	serpentinized amphibole-bearing peridotite	no	no			Porphyroclastic	A0-A1					x			x		amp
SMS_DR29_04_02	4144	serpentinized amphibole-bearing peridotite	no	no			Porphyroclastic	A1						x	x			amp
SMS_DR29_04_07	4149	serpentinized amphibole-bearing peridotite	yes	yes			Porphyroclastic	A1					x	x			x	amp-chl
SMS_DR29_07_02	4216	serpentinized amphibole-bearing peridotite	yes	-			Porphyroclastic	A1				x		x		x		amp-chl
		*all IGSN codes start by: CNRS000000																

Table A4: Amphibole composition for the four types of amphibole-bearing ultramafic samples and used for Fig. 6-8 and 10.

thin section	amphibole-bearing type	mineral	position	SiO2	TiO2	Al2O3	FeO	MnO	MgO	CaO	Na2O	K2O	Cr2O3	NiO	Cl	F	TOTAL	Mg#	Al T	(Na+K)A	Si
SMS_DR17_4_38	amphibole-bearing GSR zone	amphibole9	porphyroclast	46.68	0.35	12.03	3.72	0.09	18.67	11.61	2.67	0.04	0.46	0.11	0.07	0.00	96.50	89.94	1.37	0.65	6.63
SMS_DR17_4_38	amphibole-bearing GSR zone	amphibole10	porphyroclast	48.68	0.23	10.27	3.28	0.13	19.27	12.15	2.22	0.05	0.64	0.14	0.09	0.00	97.16	91.28	1.16	0.53	6.84
SMS_DR17_4_56	amphibole-bearing GSR zone	amphibole1	porphyroclast	52.09	0.45	6.06	3.23	0.02	20.68	12.74	1.19	0.02	0.61	0.09	0.07	0.00	97.25	91.95	0.73	0.29	7.27
SMS_DR17_4_56	amphibole-bearing GSR zone	amphibole2	porphyroclast	50.14	0.47	8.05	3.49	0.05	19.76	13.03	1.67	0.05	0.87	0.18	0.13	0.00	97.89	90.98	1.00	0.42	7.00
SMS_DR17_4_56	amphibole-bearing GSR zone	amphibole3	porphyroclast	51.38	0.36	7.42	2.97	0.03	20.11	13.08	1.53	0.01	0.87	0.10	0.12	0.00	97.99	92.34	0.87	0.36	7.13
SMS_DR17_4_56	amphibole-bearing GSR zone	amphibole4	neoblast	47.17	0.06	10.53	4.32	0.08	19.87	11.92	2.04	0.04	0.98	0.14	0.13	0.00	97.28	89.14	1.33	0.57	6.67
SMS_DR17_4_56	amphibole-bearing GSR zone	amphibole4	neoblast	48.85	0.26	10.07	3.59	0.06	19.62	13.17	1.87	0.02	0.31	0.02	0.21	0.00	98.05	90.70	1.19	0.50	6.81
SMS_DR17_4_56	amphibole-bearing GSR zone	amphibole5	neoblast	52.60	0.37	6.86	3.57	0.03	21.15	13.19	1.28	0.00	0.76	0.04	0.12	0.00	99.98	91.35	0.84	0.34	7.16
SMS_DR17_4_56	amphibole-bearing GSR zone	amphibole6	neoblast	47.36	0.66	10.98	3.67	0.00	19.00	12.71	2.04	0.03	0.84	0.13	0.13	0.00	97.56	90.22	1.34	0.55	6.66
SMS_DR17_4_56	amphibole-bearing GSR zone	amphibole7	neoblast	52.84	0.50	6.57	3.17	0.03	21.08	13.52	1.35	0.02	0.79	0.05	0.15	0.00	100.06	92.21	0.82	0.33	7.18
SMS_DR17_4_56	amphibole-bearing GSR zone	amphibole8	neoblast	51.58	0.44	6.02	2.95	0.00	20.92	12.94	1.24	0.02	0.79	0.12	0.07	0.00	97.09	92.67	0.78	0.34	7.22
SMS_DR17_4_56	amphibole-bearing GSR zone	amphibole9	post	50.36	0.39	8.30	3.37	0.01	19.59	12.92	1.46	0.07	0.47	0.10	0.06	0.00	97.11	91.19	0.94	0.37	7.06
SMS_DR17_4_56	amphibole-bearing GSR zone	amphibole10	post	54.23	0.30	4.58	2.78	0.01	21.45	12.82	0.76	0.05	0.48	0.15	0.08	0.00	97.68	93.22	0.52	0.17	7.48
SMS_DR17_4_56	amphibole-bearing GSR zone	amphibole11	neoblast	52.99	0.39	5.85	2.98	0.09	20.61	13.04	1.07	0.00	0.74	0.09	0.11	0.00	97.96	92.50	0.68	0.22	7.32
SMS_DR17_4_56	amphibole-bearing GSR zone	amphibole12	neoblast	52.10	0.42	6.93	3.43	0.03	20.35	12.99	1.25	0.05	0.73	0.11	0.13	0.00	98.51	91.36	0.81	0.29	7.19
SMS_DR17_4_56	amphibole-bearing GSR zone	amphibole13	vein	50.01	0.55	8.96	3.82	0.05	19.81	12.65	1.77	0.04	0.87	0.16	0.09	0.00	98.78	90.24	1.08	0.45	6.92
SMS_DR17_4_56	amphibole-bearing GSR zone	amphibole14	vein	49.12	0.60	9.15	3.92	0.00	19.59	12.79	1.86	0.02	1.13	0.07	0.09	0.00	98.35	89.92	1.15	0.50	6.85
SMS_DR17_4_56	amphibole-bearing GSR zone	amphibole15	vein	51.18	0.42	7.35	3.50	0.08	20.24	12.88	1.45	0.07	0.93	0.07	0.13	0.00	98.31	91.16	0.91	0.37	7.09
SMS_DR17_4_56	amphibole-bearing GSR zone	amphibole16	vein	53.40	0.37	4.91	3.01	0.00	21.50	13.17	1.15	0.03	0.85	0.14	0.10	0.00	98.63	92.72	0.66	0.29	7.34
SMS_DR17_4_56	amphibole-bearing GSR zone	amphibole17	vein	55.89	0.19	3.30	2.52	0.06	21.91	12.79	0.56	0.03	0.35	0.17	0.05	0.00	97.84	93.95	0.33	0.09	7.67
SMS_DR17_4_56	amphibole-bearing GSR zone	amphibole18	vein	55.92	0.24	3.88	2.69	0.03	22.20	13.04	0.70	0.02	0.11	0.07	0.05	0.00	98.93	93.65	0.41	0.14	7.59
SMS_DR17_4_56	amphibole-bearing GSR zone	amphibole19	vein	52.05	0.47	5.92	3.31	0.03	20.50	12.94	1.22	0.06	0.90	0.16	0.09	0.00	97.65	91.69	0.75	0.30	7.25
RS_643_4	amphibole-bearing melt-impregnated peridotite	amphibole 1	porphyroclast	48.04	0.03	10.98	3.77	0.04	20.19	12.62	2.64	0.07	0.41	0.11	0.07	0.00	98.98	90.51	1.33	0.72	6.67
RS_643_4	amphibole-bearing melt-impregnated peridotite	amphibole 2	neoblast	52.63	0.16	5.35	2.70	0.06	22.52	11.97	1.47	0.01	0.77	0.07	0.09	0.00	97.79	93.69	0.72	0.39	7.28
RS_643_4	amphibole-bearing melt-impregnated peridotite	amphibole 3	neoblast	46.13	0.01	13.33	3.86	0.12	19.69	11.63	3.20	0.15	0.21	0.03	0.10	0.00	98.46	90.10	1.56	0.86	6.44
RS_643_4	amphibole-bearing melt-impregnated peridotite	amphibole 4	porphyroclast	47.57	0.03	11.56	3.57	0.00	19.60	12.49	2.97	0.05	1.02	0.13	0.08	0.00	99.07	90.73	1.39	0.77	6.61
RS_643_4	amphibole-bearing melt-impregnated peridotite	amphibole 5	neoblast	45.54	0.22	8.87	5.36	0.00	23.15	8.90	2.31	0.12	2.81	0.14	0.05	0.00	97.46	88.51	1.49	0.66	6.49
RS_643_4	amphibole-bearing melt-impregnated peridotite	amphibole 6	neoblast	47.46	0.09	11.70	3.69	0.05	19.99	12.25	3.12	0.06	0.54	0.10	0.13	0.00	99.18	90.61	1.42	0.81	6.58
RS_643_4	amphibole-bearing melt-impregnated peridotite	amphibole 7	neoblast	47.31	0.06	11.43	3.61	0.07	20.76	11.56	2.84	0.06	0.56	0.14	0.11	0.00	98.50	91.12	1.41	0.78	6.59
RS_643_4	amphibole-bearing melt-impregnated peridotite	amphibole 8	neoblast	47.72	0.25	10.64	3.65	0.01	19.64	12.12	2.71	0.00	1.03	0.04	0.12	0.00	97.94	90.56	1.31	0.68	6.69
RS_643_4	amphibole-bearing melt-impregnated peridotite	amphibole 9	neoblast	53.50	0.10	5.59	2.78	0.00	22.06	12.57	1.83	0.04	1.00	0.07	0.08	0.00	99.63	93.40	0.72	0.42	7.28
RS_643_4	amphibole-bearing melt-impregnated peridotite	amphibole 10	neoblast	51.59	0.10	8.32	3.27	0.11	20.87	12.73	2.23	0.02	0.67	0.01	0.09	0.00	99.99	91.92	0.97	0.52	7.03
RS_643_4	amphibole-bearing melt-impregnated peridotite	amphibole 11	neoblast	51.30	0.11	7.93	2.79	0.11	20.87	12.48	2.16	0.01	0.66	0.14	0.09	0.00	98.64	93.03	0.93	0.50	7.07
RS_643_4	amphibole-bearing melt-impregnated peridotite	amphibole 12	neoblast	50.33	0.15	7.88	3.42	0.05	20.39	12.94	1.98	0.03	0.66	0.04	0.06	0.00	97.92	91.40	0.98	0.53	7.02
RS_643_4	amphibole-bearing melt-impregnated peridotite	amphibole 13	neoblast	51.64	0.18	6.60	3.57	0.00	20.61	12.87	1.99	0.06	0.67	0.12	0.09	0.00	98.39	91.15	0.84	0.48	7.16
RS_643_4	amphibole-bearing melt-impregnated peridotite	amphibole 14	porphyroclast	49.90	0.12	8.03	3.74	0.03	20.66	12.56	2.12	0.03	0.55	0.09	0.13	0.00	97.96	90.77	1.03	0.57	6.97
RS_643_4	amphibole-bearing melt-impregnated peridotite	amphibole 15	porphyroclast	49.91	0.14	7.84	3.75	0.02	20.37	12.57	2.20	0.04	0.74	0.07	0.10	0.00	97.75	90.63	1.01	0.57	6.99
RS_643_4	amphibole-bearing melt-impregnated peridotite	amphibole 16	neoblast	47.27	0.15	10.12	4.16	0.00	19.83	13.11	2.65	0.05	0.62	0.05	0.11	0.00	98.12	89.47	1.35	0.73	6.65

Table A5: Spinel composition for the four types of amphibole-bearing ultramafic samples and used for Fig. 9a-b.

Sample	amphibole-bearing type	Mineral	Position	SiO2	TiO2	Al2O3	Cr2O3	FeO	MnO	MgO	NiO	Total		Mg#	Cr#	Mg#(Fe2)
SMS_DR08_2_26	amphibole-bearing GSR zone	spinel 2	core	0.00	0.08	39.06	29.29	14.66	0.00	15.88	0.24	99.21		67.63	33.46	65.88
SMS_DR08_2_26	amphibole-bearing GSR zone	spinel 2b	core	0.04	0.05	39.54	28.37	14.72	0.00	15.51	0.20	98.42		66.41	32.49	65.27
SMS_DR08_2_26	amphibole-bearing GSR zone	spinel 2b	core	0.04	0.09	39.12	29.76	14.12	0.00	15.67	0.03	98.82		66.62	33.78	66.43
SMS_DR10_4_8A	amphibole-bearing GSR zone	spinel 1	core	0.10	0.01	48.04	19.88	14.79	0.00	15.73	0.21	98.75		64.98	21.72	65.47
SMS_DR10_4_8A	amphibole-bearing GSR zone	spinel 3	core	0.04	0.08	46.50	21.78	13.61	0.00	16.84	0.25	99.09		69.40	23.90	68.81
SMS_DR10_4_8A	amphibole-bearing GSR zone	spinel 3	core	0.08	0.12	45.93	22.52	14.00	0.00	16.46	0.24	99.35		67.84	24.75	67.70
SMS_DR10_4_8A	amphibole-bearing GSR zone	spinel 2	core	0.03	0.11	46.77	22.40	12.27	0.00	17.11	0.22	98.92		70.38	24.31	71.31
SMS_DR10_4_8A	amphibole-bearing GSR zone	spinel 2	core	0.20	0.09	42.66	25.30	14.91	0.00	15.02	0.29	98.47		63.51	28.46	64.22
SMS_DR10_4_8A	amphibole-bearing GSR zone	spinel 3	core	0.01	0.10	44.64	23.78	12.90	0.00	17.12	0.12	98.66		70.96	26.33	70.29
SMS_DR10_4_8A	amphibole-bearing GSR zone	spinel 4	core	0.03	0.11	43.84	25.45	14.03	0.00	15.90	0.08	99.43		66.14	28.02	66.90
SMS_DR10_4_8A	amphibole-bearing GSR zone	spinel 2b	core	0.03	0.14	44.66	23.90	12.91	0.00	17.33	0.09	99.06		71.39	26.42	70.53
SMS_DR17_4_6	amphibole-bearing GSR zone	spinel 1	core	0.06	0.10	39.26	27.44	16.50	0.00	15.50	0.28	99.14		66.04	31.91	62.61
SMS_DR17_4_6	amphibole-bearing GSR zone	spinel 2	core	0.03	0.06	40.27	26.06	16.56	0.00	14.60	0.18	97.75		63.00	30.27	61.13
SMS_DR17_4_6	amphibole-bearing GSR zone	spinel 1b	core	0.04	0.12	41.16	27.73	14.63	0.00	16.08	0.11	99.87		67.20	31.12	66.20
SMS_DR17_4_6	amphibole-bearing GSR zone	spinel 3	core	0.06	0.13	41.29	25.77	17.26	0.00	15.06	0.09	99.64		63.31	29.51	60.87
SMS_DR17_4_6	amphibole-bearing GSR zone	spinel 4	core	0.02	0.00	38.34	28.45	16.48	0.00	15.03	0.19	98.51		64.84	33.23	61.91
SMS_DR17_4_31	amphibole-bearing GSR zone	spinel	core	0.05	0.11	52.06	15.13	16.05	0.00	17.58	0.30	101.27		69.57	16.31	66.13
SMS_DR17_4_31	amphibole-bearing GSR zone	spinel 62	core	0.00	0.06	51.32	14.94	14.82	0.00	17.40	0.29	98.84		70.50	16.34	67.67
SMS_DR17_4_31	amphibole-bearing GSR zone	spinel 62	rim	0.00	0.03	51.74	14.61	15.41	0.00	17.19	0.40	99.38		69.56	15.92	66.53
RS_643_4	amphibole-bearing melt-impregnated peridotite	spinel	core	0.05	0.28	32.59	31.63	20.78	0.00	13.45	0.15	98.93		59.18	39.43	53.57
RS_643_4	amphibole-bearing melt-impregnated peridotite	spinel	core	0.00	0.24	37.14	28.15	18.89	0.00	14.68	0.12	99.22		62.98	33.70	58.08
RS_643_4	amphibole-bearing melt-impregnated peridotite	spinel	core	0.00	0.22	34.57	30.11	19.84	0.00	13.72	0.14	98.60		60.14	36.87	55.21
RS_643_4	amphibole-bearing melt-impregnated peridotite	spinel	core	0.02	0.03	39.20	26.59	18.34	0.00	15.04	0.17	99.39		64.12	31.27	59.38
SMS_DR29_4_6	amphibole-bearing melt-impregnated peridotite	spinel1	core1	0.02	0.40	35.96	29.91	16.93	0.00	15.01	0.18	98.40		64.85	35.81	61.26
SMS_DR29_4_6	amphibole-bearing melt-impregnated peridotite	spinel1 - RIM	rim1	0.00	0.30	34.54	31.88	17.44	0.00	14.21	0.15	98.53		62.09	38.23	59.23
SMS_DR33_2_7	amphibole mylonite	spinel1	core?	0.01	0.41	29.12	32.21	25.88	0.00	11.03	0.18	98.83		49.89	42.59	43.17
SMS_DR33_2_7	amphibole mylonite	spinel1	core?	0.02	0.32	28.48	32.63	26.75	0.00	10.32	0.17	98.69		47.17	43.45	40.76
SMS_DR33_2_7	amphibole mylonite	spinel1	core?	0.05	0.36	28.89	31.99	25.32	0.00	11.19	0.35	98.15		51.09	42.61	44.06
SMS_DR34_6_2	amphibole mylonite	spinel1	core?	0.07	0.16	29.81	34.27	21.84	0.00	11.57	0.14	97.87		52.65	43.54	48.57
SMS_DR34_6_2	amphibole mylonite	spinel1 - RIM	rim	0.00	0.21	30.03	34.67	22.64	0.00	11.56	0.15	99.26		52.05	43.64	47.67
SMS_DR04_2_9	amphibole-bearing serpentinized peridotite	spinel	core1	0.00	0.05	53.03	14.13	13.57	0.00	17.84	0.30	98.91		71.69	15.16	70.10
SMS_DR04_2_9	amphibole-bearing serpentinized peridotite	spinel	core1	0.05	0.10	53.41	14.32	13.99	0.00	17.83	0.30	100.01		70.84	15.24	69.44
SMS_DR05_6_1	amphibole-bearing serpentinized peridotite	spinel1	core1	0.00	0.12	45.84	22.11	14.74	0.00	16.43	0.30	99.54		67.91	24.44	66.53
SMS_DR05_6_1	amphibole-bearing serpentinized peridotite	spinel 1	core1	0.06	0.10	46.23	21.83	14.90	0.00	16.44	0.31	99.86		67.61	24.06	66.31

Table A6: Clinopyroxene composition for the four types of amphibole-bearing ultramafic samples and used for Fig. 9c-d.

thin section	amphibole-bearing type	mineral	position	SiO2	TiO2	Al2O3	-	FeO	MnO	MgO	CaO	Na2O	K2O	-	Cr2O3	NiO	Cl	F	Total	-	Al T	Al Oct	XMg	XCr	Ca	Na	Ti	-	Mg#	Cr#
SMS_DR10_4_8A	amphibole-bearing GSR zone	cpx 2b	core	52.55	0.18	6.08		2.38	0.23	15.22	21.23	1.05	0.02		1.41	0.07	0.00		100.43		0.106	0.152	0.912	0.13	0.82	0.07	0.00		91.20	13.47
SMS_DR10_4_8A	amphibole-bearing GSR zone	cpx 2c	core	50.64	0.27	6.16		2.23	0.08	14.70	22.00	1.02	0.00		1.52	0.03	0.00		98.65		0.134	0.134	0.919	0.14	0.87	0.07	0.01		91.89	14.17
SMS_DR10_4_8A	amphibole-bearing GSR zone	cpx 2c	core	50.58	0.23	6.18		2.29	0.00	14.82	22.22	0.98	0.00		1.59	0.01	0.00		98.91		0.139	0.129	0.920	0.15	0.88	0.07	0.01		92.01	14.72
SMS_DR10_4_8A	amphibole-bearing GSR zone	cpx 2c	core	51.71	0.22	6.20		2.39	0.10	15.36	21.22	0.96	0.02		1.62	0.06	0.02		99.87		0.124	0.141	0.917	0.15	0.82	0.07	0.01		91.66	14.90
SMS_DR10_4_8A	amphibole-bearing GSR zone	cpx	core	53.34	0.24	4.74		2.09	0.16	15.89	21.96	0.87	0.00		1.27	0.10	0.00		100.66		0.083	0.118	0.927	0.15	0.85	0.06	0.01		92.65	15.22
SMS_DR17_4_56	amphibole-bearing GSR zone	cpx 1	core	51.76	0.51	6.85		3.06	0.08	16.07	21.28	0.89	0.00		0.83	0.07	0.00		101.40		0.148	0.141	0.901	0.07	0.82	0.06	0.01		90.10	7.48
SMS_DR17_4_56	amphibole-bearing GSR zone	cpx 1	core	50.94	0.46	7.31		3.16	0.05	16.20	20.45	0.88	0.00		0.83	0.08	0.02		100.39		0.161	0.150	0.900	0.07	0.79	0.06	0.01		89.99	7.08
SMS_DR17_4_56	amphibole-bearing GSR zone	cpx 1b	core	50.26	0.43	6.90		2.75	0.04	15.28	21.93	0.68	0.04		0.90	0.05	0.00		99.26		0.159	0.139	0.907	0.08	0.86	0.05	0.01		90.70	8.02
SMS_DR17_4_56	amphibole-bearing GSR zone	opx 1	core	55.69	0.09	4.51		6.70	0.08	32.36	0.78	0.01	0.00		0.43	0.17	0.01		100.84		0.090	0.092	0.895	0.06	0.03	0.00	0.00		89.47	6.04
SMS_DR17_4_6	amphibole-bearing GSR zone	cpx 1	core - line average	52.93	0.11	5.24		2.80	0.02	16.96	19.12	1.32	0.00		1.84	0.04	0.00		100.38		0.097	0.125	0.915	0.19	0.74	0.09	0.00		91.45	19.03
SMS_DR17_4_6	amphibole-bearing GSR zone	cpx 3	core - line average	52.82	0.10	5.29		3.34	0.04	19.03	16.39	1.08	0.00		1.66	0.07	0.00		99.82		0.102	0.122	0.909	0.17	0.63	0.08	0.00		90.93	17.43
SMS_DR17_4_6	amphibole-bearing GSR zone	cpx 3	core	52.16	0.08	5.55		2.48	0.00	15.81	20.47	1.42	0.03		1.81	0.07	0.00		99.88		0.108	0.129	0.919	0.18	0.80	0.10	0.00		91.92	17.92
SMS_DR17_4_6	amphibole-bearing GSR zone	cpx 4	core - line average	53.78	0.13	4.37		2.68	0.02	17.13	19.62	1.17	0.00		1.41	0.06	0.00		100.36		0.069	0.116	0.919	0.18	0.75	0.08	0.00		91.88	17.78
SMS_DR17_4_6	amphibole-bearing GSR zone	cpx 4	core	52.17	0.15	5.52		2.20	0.03	14.61	21.69	1.41	0.00		1.97	0.00	0.00		99.75		0.102	0.135	0.921	0.19	0.85	0.10	0.00		92.11	19.36
SMS_DR17_4_6	amphibole-bearing GSR zone	cpx 4	core - line average	52.23	0.12	5.56		2.42	0.03	15.65	20.61	1.35	0.00		1.81	0.04	0.00		99.82		0.105	0.132	0.919	0.18	0.80	0.09	0.00		91.94	17.89
SMS_DR17_4_6	amphibole-bearing GSR zone	cpx 4b	core - line average	52.04	0.11	5.36		2.54	0.01	16.19	20.32	1.22	0.00		1.77	0.04	0.00		99.62		0.109	0.121	0.919	0.18	0.79	0.09	0.00		91.86	18.14
SMS_DR17_4_6	amphibole-bearing GSR zone	cpx 4c	core - line average	52.87	0.11	5.38		2.88	0.02	17.41	18.25	1.19	0.03		1.79	0.04	0.00		99.95		0.097	0.132	0.915	0.18	0.70	0.08	0.00		91.46	18.24
RS_643_4	amphibole-bearing melt-impregnated peridotite	cpx 2	core	50.14	0.21	8.42		3.06	0.08	15.26	22.61	0.79	0.01		0.78	0.03	0.06		101.43		0.198	0.159	0.897	0.06	0.87	0.05	0.01		89.68	5.82
RS_643_4	amphibole-bearing melt-impregnated peridotite	cpx 2	core	51.64	0.16	6.43		2.94	0.02	16.12	22.41	0.74	0.02		0.62	0.08	0.08		101.26		0.146	0.126	0.907	0.06	0.86	0.05	0.00		90.65	6.11
SMS_DR33_2_1	amphibole mylonite	cpx3	core	52.63	0.55	3.23		5.64	0.18	16.42	20.97	0.60	0.01		0.28	0.02	0.00	0.04	100.57		0.08	0.06	0.83	0.06	0.82	0.04	0.02		83.41	5.58
SMS_DR33_2_1	amphibole mylonite	cpx3	core	53.18	0.49	2.93		6.21	0.22	16.86	19.78	0.57	0.02		0.30	0.07	0.00	0.00	100.63		0.07	0.06	0.82	0.07	0.77	0.04	0.01		82.37	6.51
SMS_DR04_2_9	amphibole-bearing serpentinized peridotite	opx1	core	54.66	0.10	5.85		6.55	0.07	32.08	0.74	0.03	0.01		0.64	0.07	0.00	0.08	100.88		0.13	0.11	0.90	0.07	0.03	0.00	0.00		89.62	6.86
SMS_DR04_2_9	amphibole-bearing serpentinized peridotite	opx1	core	54.25	0.09	5.78		7.07	0.15	31.42	0.77	0.03	0.03		0.83	0.04	0.00	0.06	100.52		0.13	0.11	0.89	0.09	0.03	0.00	0.00		88.57	8.81
SMS_DR05_6_1	amphibole-bearing serpentinized peridotite	opx1	core	55.04	0.05	4.57		6.02	0.07	32.57	0.81	0.06	0.01		0.76	0.15	0.03	0.00	100.14		0.10	0.08	0.91	0.10	0.03	0.00	0.00		90.51	10.09
SMS_DR05_6_1	amphibole-bearing serpentinized peridotite	opx1	core	55.86	0.09	4.33		5.76	0.04	32.79	0.66	0.03	0.01		0.88	0.06	0.02	0.06	100.59		0.09	0.09	0.91	0.12	0.02	0.00	0.00		90.96	11.97
SMS_DR29_4_2	amphibole-bearing serpentinized peridotite	cpx1	core	55.72	0.01	0.10		2.13	0.04	17.77	25.61	0.02	0.00		0.00	0.02	0.00	0.00	101.43		0.00	0.00	0.94	0.00	0.98	0.00	0.00		93.59	0.00
SMS_DR29_4_2	amphibole-bearing serpentinized peridotite	cpx2	core	55.36	0.05	0.04		2.88	0.16	17.20	25.05	0.00	0.01		0.01	0.06	0.02	0.00	100.85		0.00	0.00	0.91	0.15	0.97	0.00	0.00		90.96	15.12

SUPPLEMENTARY FIGURES

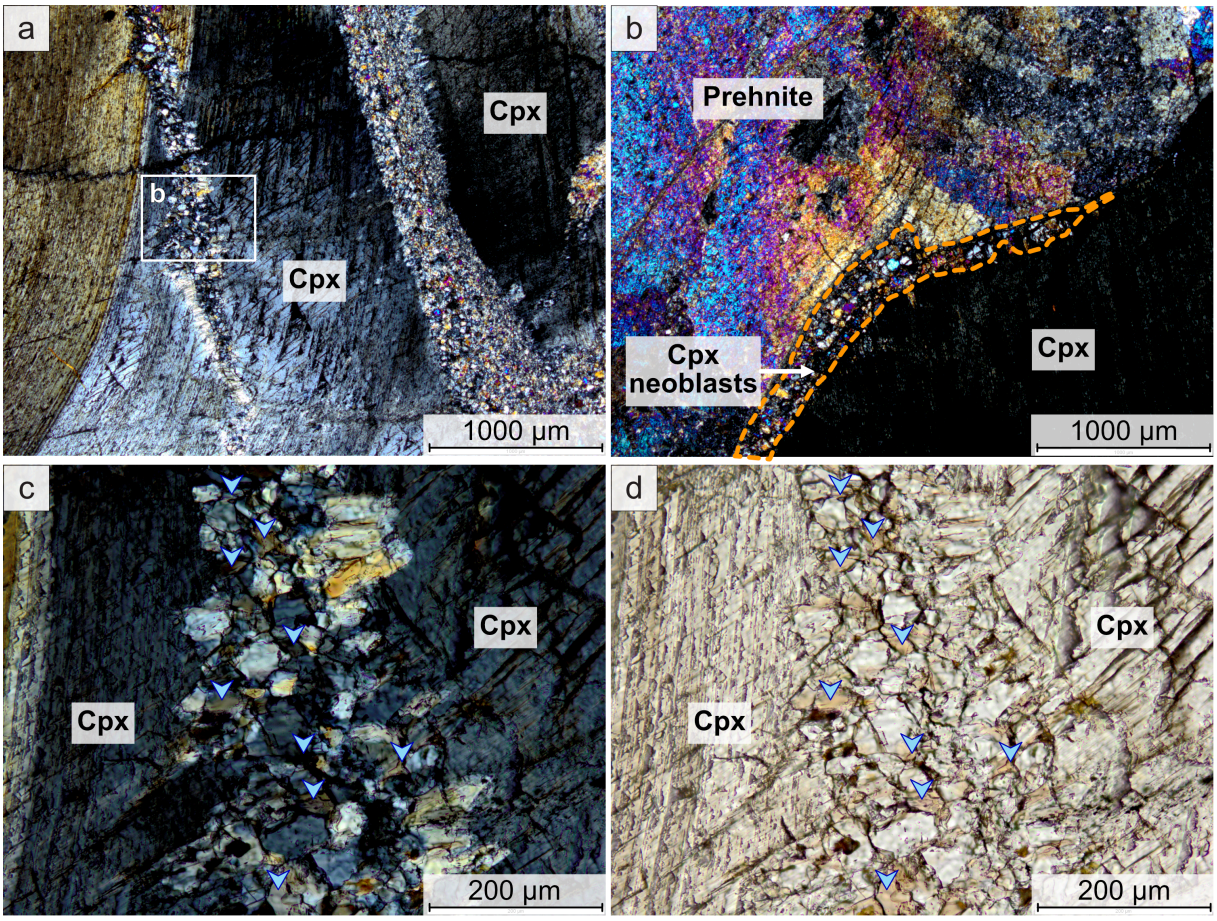

Figure A1: Microphotographs under cross-polarized light (a-c) and natural light (d) of amphibole in an amphibole-bearing mylonite (SMS-DR33-2-01). (a) Coarse, ductilely deformed and partially recrystallized porphyroclasts of clinopyroxene (Cpx). (b) Large prehnite grains coexisting with clinopyroxene. Recrystallization occurs along the two-phase grain boundaries. (c-d) Detail of (a) showing neoblasts of clinopyroxene recrystallizing together with brown amphibole (pointed by blue arrows) .